Identification of a robust and durable FeN_4C_x catalyst for ORR in PEM fuel cells and the role of the fifth ligand

Identification of a robust and durable FeN_4C_x catalyst for ORR in PEM fuel cells and the role of the fifth ligand

Parisa Nematollahi,[*,1] Bernardo Barbiellini,[2,3] Arun Bansil,[3] Dirk Lamoen,[4] Jia Qingying,[5] Sanjeev Mukerjee,[5] and Erik C. Neyts[1]

[1] Research Group PLASMANT, NANO lab Center of Excellence, Department of Chemistry, University of Antwerp, Universiteitsplein 1, B-2610 Wilrijk-Antwerp, Belgium

[2] Department of Physics, School of Engineering Science, LUT University, FI-53851 Lappeenranta, Finland

[3] Department of Physics, Northeastern University, Boston, MA 02115, USA

[4] EMAT & NanoLab Center of Excellence, Department of Physics, University of Antwerp, B-2020 Wilrijk-Antwerpen, Belgium

[5] Department of Chemistry and Chemical Biology, Northeastern University, Boston, MA 02115, USA

* Corresponding author. **Phone:** (+32) 32652346. **E-mail**: parisa.nematollahi@uantwerpen.be

Abstract

Although recent studies have advanced the understanding of pyrolysed Fe-N-C materials as oxygen reduction reaction (ORR) catalysts, the atomic and electronic structure of the active sites and their detailed reaction mechanisms still remain unknown. Here, based on first-principles Density Functional Theory (DFT) computations, we discuss the electronic structures of three FeN_4 catalytic centers with different local topologies of the surrounding C atoms with focus on unraveling the mechanism of their ORR activity in acidic electrolytes. Our study brings back a forgotten, synthesized pyridinic Fe-N coordinate to the community's attention, demonstrating that this catalyst can host an excellent activity for promoting direct four-electron ORR through the addition of a fifth ligand such as $-NH_2$, $-OH$, and $-SO_4$. We also identify sites with good stability properties through the combined use of our DFT calculations and Mössbauer spectroscopy data.

Keywords: Oxygen reduction, Fuel cell, Mössbauer spectroscopy, Fe-N-C, FeN_4, density functional theory, functional ligand, non-PGM catalysts

Introduction

Non-noble-metal catalysts for oxygen reduction reaction (ORR) are of interest in major clean technologies such as the metal-air batteries and polymer-electrolyte-membrane fuel cells (PEMFCs) [1]. M-N_4 active sites (M=Fe, Co, Cu, Ni) adsorbed on C-based supports have been shown to be promising catalysts for ORR in acidic medium [2-5]. However, these catalysts exhibit rapid degradation at the cathode in acidic pH. Their highest electrocatalytic activity occurs at pyrolytic temperatures of 773 to 973 K at which a catalytic M-N_4 site binds to the carbon support [6-9]. The M-N_4 site is considered a low-temperature catalytic site [8] for pyrolytic temperatures of 773 to 973 K and a high-temperature catalytic site [10, 11] above 1073 K. Many efforts have been made to determine the detailed structural properties of the catalytic FeN_4 site at high temperatures.

Dodelet et al. [12, 13] prepared three catalysts for ORR by pyrolyzing two iron precursors (Fe^{II} acetate and Fe porphyrin (Cl-Fe^{III} TMPP)) adsorbed on a carbon support between 400-1000 $C°$. They found that the Fe–N–C material always contains two types of catalytic sites: (i) FeN_2/C as the high-temperature catalytic site (HT) and (ii) FeN_4/C as the low-temperature (LT) catalytic site, whose relative proportions depend on the pyrolysis temperature and the precursor used. The most representative ion for the HT site is $FeN_2C_4^+$, see Figure S1a in the Supplementary Information, while for the LT site, it is $FeN_4C_8^+$ [14] (Figure S1b). Dodelet et al. [12, 13] thus proposed that FeN_2/C is electrocatalytically more active than FeN_4/C and that both sites emanate from high Fe porphyrin loading. A Fe–N_{2+2}/C type active center that forms by bridging two graphene platelets with an iron ion was subsequently identified [8, 15-17] where each graphene platelet is similar to the proposed structure shown in Figure S1a. Mössbauer spectroscopy has also shown a similar configuration for Fe–N_{2+2}/C [18]. Unlike $FeN_4C_8^+$ (Figure S1b), with Fe-N pyrrolic coordination, Fe in Fe–N_{2+2}/C (Figure S1c) exhibits

2

pyridinic Fe-N coordination. More importantly, Fe–N_{2+2}/C and $FeN_4C_8^+$ have been proposed as fully coordinated Fe–N_2/C and the known Fe–N_4/C site, respectively. However, the structure of the fully-coordinated Fe–N_{2+2}/C is unknown.

The vital role of carbon support on the ORR activity of the electrocatalysts has been well recognized [19-21]. In 2008, Charreteur et al. [22] proposed a structure for most FeN_x/C active sites based on their earlier Fe–N_2/C and FeN_4/C structures (Figure S2). One year later, Lefèvre et al. [23] produced microporous carbon-supported Fe-based catalysts. They believed that the active sites containing Fe cations coordinated by pyridinic nitrogen functionalities were located in the interstices of graphitic sheets within the micropores. In 2015, Zitolo et al. [24] synthesized Fe-N-C materials and studied their structures pyrolysed in Ar or NH_3. Using X-ray absorption near-edge spectroscopy (XANES), they studied the structure of active sites in Fe-based catalysts. The HT pyrolysis was used to prepare a catalyst from iron, nitrogen, and carbon as precursors leading to the formation of graphene sheets in which iron atoms are coordinated by nitrogen atoms, thereby doping the carbon support. In Figure S3, three different FeN_4C_x structures with different numbers of local carbon atoms are shown: (i) a pyridinic FeN_4 moiety bounded in a graphene sheet (FeN_4C_{10}), (ii) the FeN_{2+2} moiety bridging two graphene sheets (FeN_4C_8), and (iii) an iron-doped porphyrinic configuration (FeN_4C_{12}). By modeling the XANES spectra, Zitolo et al. [24] concluded that the correct structure is a FeN_4C_{12} moiety in which the FeN_4 active site bridges two graphene sheets, so that the formed catalytic sites are based on a porphyrinic architecture, and not the previously considered pyridinic structure.

Ideally, the ORR could proceed on either sides of the active site. However, because of the low-coordination environment of the isolated Fe atom, it is possible that it adsorbs electrolyte ions or molecules from the electrocatalysis solution system. Effects of the coordination environment on ORR [25, 26] and the presence of a functional ligand on one side of the FeN_4/C catalyst along with the effects of different functional ligands on ORR activity have been discussed in

3

recent theoretical and experimental studies [27-29]. For instance, Jia et al. [30] demonstrated that the pyridinic FeN_4 structures remain ORR active, especially the FeN_4C_8 catalyst. They suggested that the presence of a fifth ligand (i.e., an NH_2^-) may cause a significant increase in ORR activity. Changing the oxidation state of Fe was then suggested to be accompanied by a decrease in Fe-N bond distance during the ORR reaction as measured by in-situ extended X-ray absorption fine structure (EXAFS) for a highly ORR active Fe-N-C catalyst. Using DFT calculations they predicted an increase in ORR activity with ligand vs. ligand-free configurations and showed that the ORR activity is governed by the dynamic structure associated with the $Fe^{II/III}$ redox transition rather than the static structure of the base sites.

To make the Fe-N-C catalysts suitable for industry, their stability and activity should be enhanced. To reach this goal, it is necessary to understand the detailed reaction mechanisms that occur at the surface of these catalysts. Also, it is important to determine the relation between the Fe-N-C catalysts, the spin-state and the orbital configuration of the surrounding N atoms. This can be determined by X-ray emission (XES) [31] or Mössbauer spectroscopy [32, 33] as an indication of the metal centers [34]. Recently, it was revealed by ex-situ ^{57}Fe Mössbauer spectroscopy that Fe-N-C catalysts consist of two types of FeN_x sites, labeled D1 (doublet with quadrupole splitting (QS) values of 0.9-1.2 mm.s^{-1}) and D2 (QS = 1.8-2.8 mm.s^{-1}) with the same isomer shift [35, 36]. In 2019, Mineva et al. [37] applied Mössbauer spectroscopy to interpret the doublets for the Fe-N-C catalysts and determined the Fe oxidation number and spin states of FeN_4 structures for two different local carbon topologies (FeN_4C_{10} and FeN_4C_{12}). The combined theoretical and experimental results identified that the FeN_4 sites are mainly in Fe^{II} low-spin and Fe^{III} high-spin states. They assigned the experimental doublet D1 to $Fe^{III}N_4C_{12}$ in high-spin with the calculated quadrupole splitting energy of $\Delta E_{QS} = 0.9-1.2$ mm.s^{-1} and the experimental doublet D2 to $Fe^{II}N_4C_{10}$ with low- and medium spin and $\Delta E_{QS} = 2.5-3.3$ mm.s^{-1}. Finally, they reported that the D1 sites may be more active for ORR because

they correspond to surface-exposed sites, while D2 may correspond to either the bulk sites, which are inaccessible to O_2 during the ORR, or to the surface sites that bind O_2 more weakly than D1. Using Mössbauer spectroscopy, Li et al. [38] indicated that Fe-N-C catalysts comprise two distinct FeN_4 sites, the high-spin S1 site, and the low- or medium- spin S2 site. They noticed that these two sites embed differently into the C matrix, and claimed that the oxidation number of Fe in the S1 site switches from II to III in the range of 0-1 V, while S2 does not change and stays as Fe^{II}. They concluded that although both active sites contribute to the ORR in an acidic medium, the S1 site degrades quickly to ferric oxide Fe(III), while S2 is more durable with no degradation after 50 h of operation at 0.5 V.

Here, we characterize the active sites in FeN_4 catalysts by using our DFT simulations along with [57]Fe Mössbauer spectroscopy data, and discuss how the ORR activity can be enhanced on the porphyrinic (FeN_4C_{12}) and pyridinic (FeN_4C_8, FeN_4C_{10}) structures. We thus demonstrate that the presence of the fifth ligand changes the oxidation state of the Fe atom, which leads to a substantial enhancement of the ORR activity. This remarkable increase is more visible on the pyridinic FeN_4C_8 compared to the porphyrinic FeN_4C_{12} structure. Our study opens a new pathway for finding a broader combination of functional ligands and metal centers for improved ORR activity.

2. Computational method

DFT calculations were carried out using the Vienna ab initio simulation package (VASP) [39-41] using a projector-augmented-wave (PAW) method [42] with cut-off energy of 400 eV. Perdew-Burke-Ernzerhof (PBE) [43] functional is used for treating exchange-correlation effects. The zero-damping Grimme approximation, DFT-D2, is used to compute the weak dispersion interactions [44]. (The use of DFT-D3 dispersion [45] was found to yield only small changes in the reaction coordinates of the order of 0.05 eV). All calculations are spin-polarized. The convergence criterion for the residual force and energy in structural relaxations was set to

0.01 eV/Å and 10^{-6} eV, respectively. Atomic charges and charge transfer were calculated from the Bader charge scheme [46]. For the Fe atoms, the pseudopotential used includes 3s and 3p states as valence states in all calculations. Details of DFT calculations and model simulations, free energy calculations, and Mössbauer computations are given in the Supporting Information.

3. Results and discussion

3.1. Structural characterization of pristine FeN$_4$ electrocatalysts

First, we investigate the geometry and binding energy of each FeN$_4$ site displayed in Figure 1. The pristine FeN$_4$ catalysts have a D$_{4h}$ symmetry with a completely planar structure. Therefore, all six electrons can be associated with the Fe atom where the Fe atom is in an oxidation state of Fe(II) [47]. According to our DFT calculations, the adsorption energy of the Fe atom into the N$_4$ pyridinic and porphyrinic cavities is very high (see Table S1), especially in complex 1c, suggesting that the Fe atom anchors very strongly into the N$_4$ defective site leading to the high stability of the formed catalysts. The calculated Fe−N bond lengths of the optimized complexes are in the range of 1.85−1.97 Å which is in close agreement with previous studies [30, 48, 49].
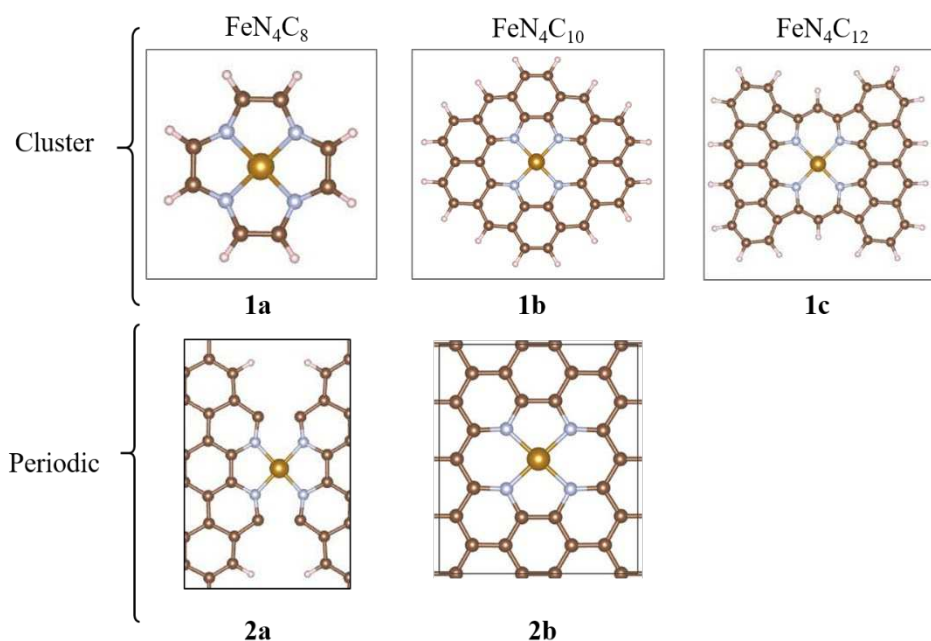

Figure 1. Proposed FeN$_4$C$_x$ (x = 8, 10, and 12) structures as representative Fe-N-C materials. The optimized 1a, 1b, and 1c structures are considered to be classified in the cluster group while the 2a and 2b structures are sorted in the periodic group. Color code: brown, C; blue, N; orange, Fe; white, H.

The calculated decomposed total density of states (DOS) for all the complexes is shown in Figure S5. The calculated HOMO-LUMO energy gap for pure 1a, 1b, and 1c clusters are 1.40, 0.21, and 0.19 eV, respectively.

3.2. ORR on four-fold-coordinated FeN$_4$ catalysts

Adsorption of ORR species. The ORR in an acidic environment starts with the adsorption of an O$_2$ molecule on the surface followed by four hydrogenation steps, forming the *OOH. The *OOH then reacts with the second (H$^+$ + e$^-$) from the solvent and forms the *O while an H$_2$O molecule is released from the surface. Subsequently, the third protonation of *O results in the formation of an *OH species. Finally, the last proton-electron pair combines with *OH and produces another H$_2$O above the FeN$_4$ active site. All possible orientations for each adsorbate (except for atomic oxygen *O) have been considered and the energetically favorable structures are shown in Figures 2 and S6. The oxygen molecule adsorbs through end-on orientation on all complexes except on complex 1a in which it tends to have a side-on orientation in agreement with other investigations [50, 51]. The O−O bond (d$_{O-O}$) increases by about 13% in complexes 1a and 6.8% in complexes 2b and 1c after O$_2$ adsorption, suggesting charge transfer from Fe to the 2π* orbitals of the adsorbed oxygen (Table S1). Besides O−O bond elongation, d$_{Fe-N}$ increases by about 2% in complex 1a while it increases only 0.5% in complexes 2b and 1c.
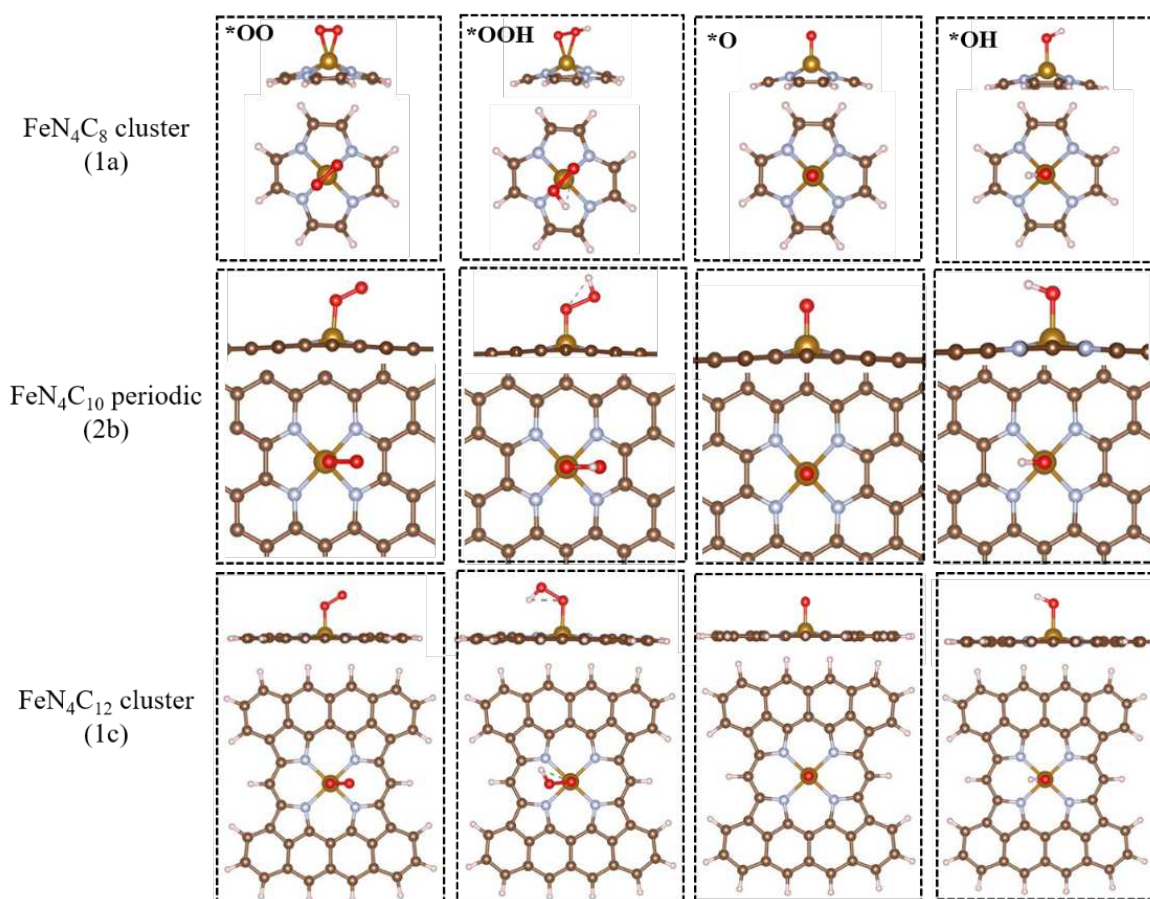
Figure 2. The most stable optimized configurations of ORR intermediate species adsorbed on complexes 1a, 2b, and 1c. Color code: brown, C; blue, N; orange, Fe; white, H; and red, O.

The Gibbs free energy of each reaction step greatly depends on the total energy difference between the two intermediate products. Consequently, the performance of the reaction corresponds to the adsorption behavior of the intermediates on the catalysts. As expected, the adsorption of *OH outcompetes that of *O_2 and *OOH. Moreover, the adsorption energy of *O is smaller than that of *OOH (Figure S7). The computed adsorption energy of *O_2 on complexes 2b and 1c are reported in Table S2. These values are comparable to the commonly used catalyst in PEM, Pt(110), with E_{ads} = -1.10 eV. The adsorption energy of *O_2 on complex 1a and 2a is high (more negative), E_{ads} = -2.90 and -2.02 eV, respectively, which is higher than the values reported by Lie et al. [50] (-1.67 eV) or Kattel et al. [52] (-1.61 eV). The small difference between the computed adsorption energy of *O_2 on complexes 1a and 2a might be related to the small size of the complex 1a which leads to exaggerated binding energy while in

a similar periodic system, the values are more moderate. However, the same trend can be seen for the adsorption of intermediates on complex 2a (see Figure S7). The DOS plots of *OH adsorbed on FeN$_4$ complexes also indicate a strong interaction between the Fe-d$_{yz}$ and O-p$_y$ orbitals in complexes 1a and 2b (Figure S8). At the HOMO level, the interaction of the Fe-d_{z^2} and O-p$_z$ orbitals are visible in complex 1c which might explain the half-filled d orbitals after *OH adsorption [53]. However, one can see that upon the adsorption of *OH intermediate, the HOMO-LUMO energy gap increases in complexes 1a, 1b, and 1c to 1.91, 1.71, and 0.29 eV, respectively.

Electrochemical ORR. A four-electron pathway of ORR in acidic media, $* + O_2(g) + 4(H^+ + e^-) \rightarrow 2H_2O$, is known as the ideal reaction [54] as discussed in the Supporting Information. Upon the adsorption of ORR species on the active Fe center on pristine FeN$_4$ catalysts, the symmetry of the structure changes. The open-shell nature of the interacting ORR species with the Fe^{II} atom of the pristine FeN$_4$ catalyst describes the change of iron oxidation number from Fe^{II} to Fe^{III} [27, 47, 55]. In addition, during the ORR, the four equatorial Fe$-$N bond lengths of each complex, which were identical in the pristine FeN$_4$ complexes, increase and divide into two pairs with different bond lengths that cause the Fe out-of-plane displacement. Changes in the average Fe$-$N bond length are monitored during the reduction reaction on all five catalysts. As is clear from Table S1, the Fe$-$N distance increases by about 0.5-2% during the ORR, depending on the catalyst [30, 56]. This reduces the stability of the catalyst as in O$_2$-saturated electrolyte, the activity and the number of active FeN$_4$ sites decreases, forming iron oxide particles during cycling [38, 57]. This originates from the strong attraction of ORR species with the Fe active center as reported in Table S1. One can see that the Fe-O bond length of adsorbed ORR species on complexes 1a, 2a, 2b, and 1c is in the range of 1.61<d$_{Fe-O}$<1.88 Å, confirming the strong adsorption of oxygenated species on Fe atom. This further leads to a significant protrusion of the Fe atom from the N-plane, i.e., a movement of about 0.3 Å in

complexes 1c and 2b that is in good agreement with other five-fold-coordinated TM complexes (ML$_5$) [58], Fe-porphyrine structure [47], and is more pronounced in complex 1a with a value of about 0.9 Å. The distinct Fe displacement and Fe−N switching behavior is also shown theoretically and confirmed experimentally [30].

Since the calculated results for complexes 1b and 2b were similar, we chose complexes 1a, 2a, 2b, and 1c for calculating the ORR to reduce computational costs. The calculated ORR reaction coordinate for each complex at zero potential is plotted in Figure 3. The ideal pathway (shown in black) is the ORR standard reversible potential (1.23 V). Several important conclusions can be derived from this analysis: (i) the calculated limiting potential (U$_{lim}$) for ORR on complexes 1a, 2a, 2b, and 1c is -0.42, -0.11, 0.25, and 0.55 V vs reverse hydrogen electrode (RHE), respectively (see Table S1). The uphill ORR steps for complex 1a and 2a are related to the formation of H$_2$O(g); (ii) being closer to the ideal line, complex 1c shows better but not very high catalytic activity for ORR; (iii) complexes 1a and 2a with the lowest local C coordination have the lowest tendency for catalyzing ORR. The reason might be related to the larger Fe^{III} out-of-plane displacement in these catalysts. To avoid expensive calculations, complex 1a is chosen as a representative of the FeN$_4$C$_8$ and used in futher calculations. According to the calculated binding energies of the ORR species on each catalyst, we can conclude that the adsorption of these species becomes stronger with decreasing number of local carbon atoms around the FeN$_4$ center (Table S2), requiring more energy for the cleavage of the bonds and formation of two water molecules, in close agreement with previous investigations [24, 50].
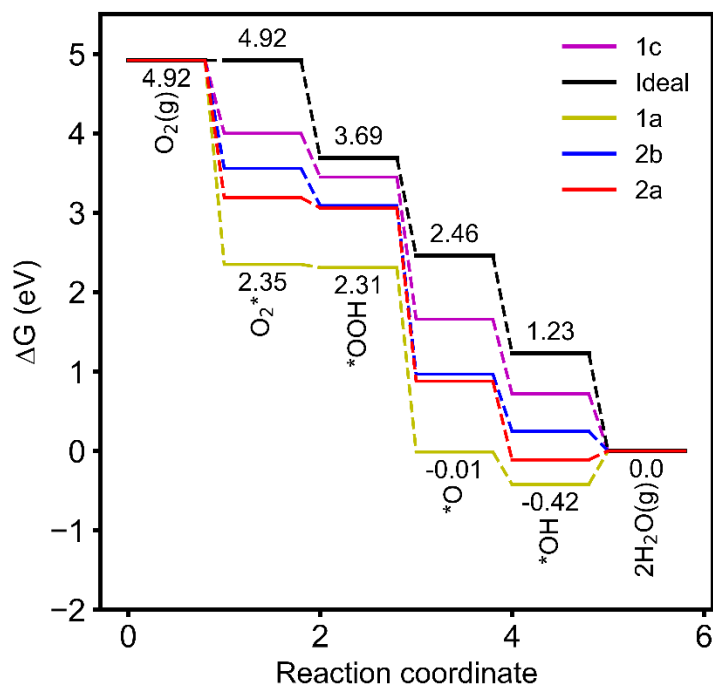
Figure 3. Free energy diagram of the ORR on complexes 1a, 2a, 2b, and 1c with an active Fe^{III} center

3.4. ORR on five-fold-coordinated FeN$_4$ catalysts

Adsorption of ligands. Subsequently, we determined the ORR activity of the studied complexes in the presence of three different ligands, i.e., NH_2^-, OH^-, and SO_4^{2-}, which come from the precursors, the ORR intermediate with a high tendency to poison the FeN$_4$ active sites, and the H$_2$SO$_4$ electrolyte, respectively. The structural changes induced by the ligands on the FeN$_4$ catalysts are similar to those shown in Figure 2 considering that the protrusion of the Fe^{III} atom from the N-plane is more pronounced in complexes 1a and 2a (Figure S9). For adsorption of the SO_4^{2-} ion on Fe^{II}, two adsorption orientations are considered. One in which the SO_4^{2-} ion binds to the Fe atom with one oxygen, and the other, in which the SO_4^{2-} binds with two oxygen atoms, thus forming either one or two Fe-O bonds. We demonstrate in Figure S10 that regardless of the type of complex and its unit cell, SO_4^{2-} binds stronger than OH^- and NH_2^- ligands on all FeN$_4$ centers. However, all the ligands adsorb on the FeN$_4$C$_8$ catalyst with much higher adsorption energies (more negative) than that of other studied complexes (Table S3).

11

Adsorption of ORR intermediates. Figure S11 shows the optimized six-fold coordinated FeN4 catalysts in which the ORR intermediate species adsorbs on the FeN4 in the presence of the fifth ligand (FeN4C-ligand). It can be seen that the symmetry of the iron atom in the configurations changes to octahedral and the oxidation state of the Fe atom reduces from Fe^{III} to Fe^{II} [33, 47], restoring the planarity of the FeN4 section. As reported in Table S1, the d_{Fe-N} within the pyridinic and porphyrinic N4 sites expand slightly, but this increase is negligible compared with that of ORR on ligand-free complexes. The reason is that the fifth ligand in these structures pulls back the Fe atom into the plane upon the adsorption of the ORR intermediates on the five-fold coordinated FeN4 sites preventing the elongation of the Fe-N bond. In contrast, d_{Fe-O} increases significantly compared to its value in ligand-free complexes. The Fe-O bond elongation induced by the presence of the fifth ligand reduces the adsorption energy of the $*O_2$, $*OOH$, $*O$, and $*OH$ intermediate species, as shown in Figure S12 and reported in Table S3, contrary to the ligand-free catalysts. This is seen especially in complex 1a and it facilitates the ORR in agreement with reports by Holby et al. [27].

Electrochemical ORR. Following the observation that a greater Fe displacement leads to a lower ORR activity in the ligand-free complexes, we find that the presence of the fifth ligand on the studied catalysts and specifically on complex 1a drastically increases their electrocatalytic ORR activity. In addition, there is a significant elongation of the Fe-O distance, especially if the first ORR step is the adsorption of oxygen. The elongation amounts to about 6-18% in complex 1a and about 10-13% in complex 2b (see Table S1). In complex C, this elongation is in the range of 1-2%. The Fe-O bond length of other intermediates adsorbed on the studied complexes changes between $6\% < \Delta d_{Fe-O} < 1\%$. Interestingly, we noticed that the highest Fe-O distance is for the complexes with the NH_2 and OH ligands.

The free energy plot of the ORR on complexes 1a, 2b, and 1c is shown in Figure S13. Our results reveal that in the presence of the fifth ligand, the four-electron ORR proceeds with

smaller limiting potentials (U_{lim} = -ΔG_{min}/e), closer to the ideal pathway (see Table S1). Along the ORR pathways on complex 1a, the calculated ORR free energy diagram in Figure S13a shows that the adsorption of O_2, $O_2(g) + 4(H^+ + e^-) \rightarrow *O_2 + 4(H^+ + e^-)$, on the Fe center in the presence of SO_4 ligand is endothermic with ΔG_{min} = 0.45 eV. O_2 adsorption on the Fe active center of complex 1a in the presence of OH and NH_2 ligands is the ORR potential determining step (PDS) with ΔG_{min} of -0.07 and -0.19 eV, respectively, showing that this step is thermodynamically spontaneous under ambient conditions. ORR steps on complex 2b, shown in Figure S13b, are all downhill and thermodynamically favorable. The calculated PDSs in the presence of SO_4, OH, and NH_2 are related to O_2 adsorption, second H_2O formation, and the first hydrogenation step of $*O_2$ to $*OOH$, respectively. Similar to complex 2b, the ORR on complex 1c is also thermodynamically exergonic and the PDSs are related to the second H_2O formation and the first hydrogenation step of $*O_2$ to $*OOH$, in the presence of SO_4/OH and NH_2, respectively.

Our analysis confirms that FeN_4 catalysts catalyze the four-electron ORR more actively in the presence of NH_2 and OH ligands, see the free energy profiles for various reaction steps in Figure S13.

According to our investigation, we confirm that the FeN_4 catalysts catalyze the four-electron ORR more actively in the presence of NH_2^- or OH^- ligand by computing the free energy profile for each reaction step on all studied catalysts (Figure S13). One can see that amongst the different ligands, the addition of NH_2^- to FeN_4 complexes decreases the adsorption energies of the ORR intermediates (Figure S12) and thereby drastically increases their ORR activity. Our results are in good accordance with previously reported experimental and theoretical results, reporting that the presence of a fifth ligand makes the catalyst ORR active [59, 60]. Thus, in contrast to what was reported in recent studies [24, 37, 38, 61], we here show that FeN_4C_8 can promote the electrocatalytic ORR with lower limiting potential than that of FeN_4C_{10} and

FeN$_4$C$_{12}$ (see Figure 4). As proposed by Dodelet [12], we hereby confirm that Fe^{II} is a representative ion of the robust FeN$_4$C$_8$ catalyst toward ORR at 0V potential.
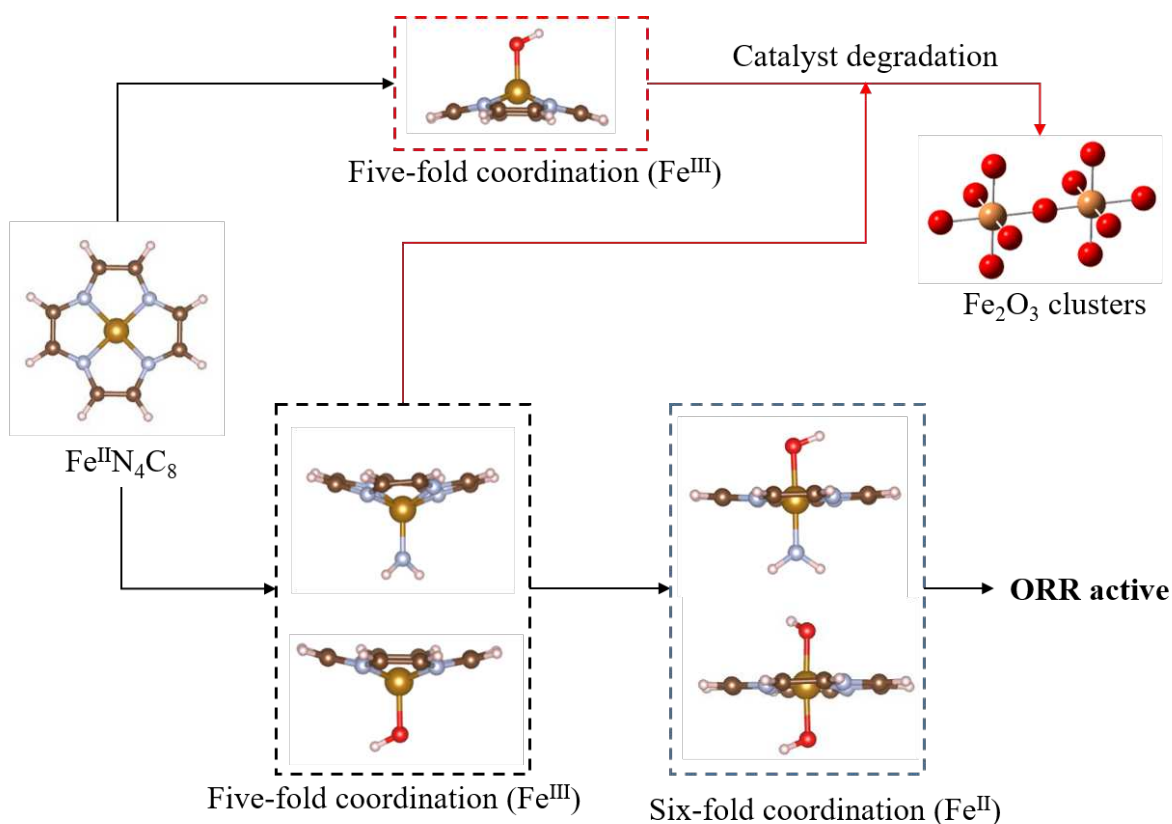

Figure 4. An atomistic visualization of the ORR on the FeN$_4$C$_8$ catalyst in an acidic medium. During the reduction process, the four-fold coordination Fe^{II}N$_4$C$_8$ switches to five-fold coordination Fe^{III}N$_4$C$_8$ leading to catalyst degradation and formation of ferric oxide. In the presence of the fifth ligand, the ORR activity of the catalyst increases significantly. The oxidation number of iron does not change in the six-fold coordination structure. Color code: brown, C; blue, N; orange, Fe; white, H; and red, O.

According to the calculated magnetic moment (***μ***) reported in Table 1, one can see that the magnetic moment of Fe decreases with the addition of NH$_2^-$ as the fifth ligand while it increases upon adsorption of OH$^-$ and SO$_4^{2-}$ ligands. It is known that the change of the magnetic moment stems from the change of spin configuration [62]. The magnetic moment of Fe decreases in the ligand-free catalyst after adsorption of ORR intermediates except for the adsorption of *OH. The decrease in the magnetic moment of the Fe atom is also visible in complex 1a-NH$_2$ except for adsorption of *OOH and *OH, for which the μ are higher than those in the pure complex 1a-SO$_4$. In complexes 1a-OH and 1a-SO$_4$ the magnetic moment decreases for all the

intermediates adsorbed on the catalyst. The magnetic moment of the Fe atom in other complexes is reported in Table S4.

Table 1. The calculated magnetic moment (in units of the Bohr magneton μ_B) of iron atom in complex 1a for ORR configurations with and without the fifth ligand. Values in parenthesis correspond to the calculated total magnetic moment of the complex.

Complex	1a	1a-NH$_2$	1a-OH	1a-SO$_4$
Substrate	1.70 (2)	0.74 (1)	2.03 (3)	0.00 (0)
***OO**	1.19 (2)	0.04 (1)	0.47 (1)	0.00 (0)
***OOH**	0.80 (1)	1.30 (2)	1.36 (2)	1.11 (1)
***O**	0.00 (0)	0.67 (1)	0.67 (1)	0.84 (2)
***OH**	2.03 (3)	1.41 (2)	1.49 (2)	1.35 (1)

3.5. Linking ^{57}Fe Mössbauer spectroscopy to the Fe oxidation state

^{57}Fe Mössbauer spectroscopy has been extensively used to determine the local electronic structure, coordination of iron nuclei, and magnetic properties in many materials containing Fe atoms in their active sites [63-65]. The ΔE_{QS} is an important Mössbauer parameter originating from the hyperfine interactions between the Fe nucleus and its surrounding electronic environment. It is known that changing the iron oxidation state, spin state, or chemical surrounding has a substantial effect on ΔE_{QS} [66]. Therefore, we used this technique to characterize the different oxidation states of iron in the studied complexes 1a, 2b, and 1c.

ΔE_{QS} is calculated for three sets of complexes: (i) ligand-free (pure) complexes that contain a significant fraction of ferrous moieties, Fe^{II} (four-fold coordinated); (ii) complexes containing the ferric ion, Fe^{III}, which is modeled by adsorbing either an ORR species or ligand on the Fe center (five-fold coordinated); and (iii) Fe^{II}N$_4$ with six-fold coordination. Since our results are in close agreement with those reported for similar Fe-N-C structures [24, 37], we believe our results are accurate for the proposed FeN$_4$C$_8$ structures, too.

First, we focus on the pure catalysts containing the Fe^{II} in a low or medium-spin state. In Figure 5 we schematically show the ΔE_{QS} values for the FeN$_4$ complexes calculated using DFT with a combination of five available spin states Fe^{II} (S = 0), Fe^{II} (S = 1), Fe^{III} (S = 1/2), Fe^{III} (S = 3/2), and Fe^{III} (S = 5/2). The corresponding combinations are taken based on Mössbauer experiments,

vis. Fe^{II} (S= 0) and Fe^{III} (S = 5/2) for the Fe−N−C catalysts. We did not consider the high-spin state (S=2) because the obtained Mössbauer parameter values for this spin state were never experimentally observed for Fe-N-C catalysts [35, 67].

Our DFT calculations indicate that the ΔE_{QS} for pure FeN_4 catalysts with either a closed-shell (S=0) or an open-shell (S=1) structure is in the range of 2.5−3.2 mm.s^{-1}, see rows 1−3 in Table S5. As shown in Figure 5 and reported by Mineva et al. [37], the obtained ΔE_{QS} values for complexes containing ferrous moieties with S=0 spin state are in the range of the experimental ΔE_{QS} values reported for $Fe^{II}N_4$ moieties. One can see in Table S5 that in the pure catalysts there is a clear difference between the ΔE_{QS} values of the complex 1c (2.5 mm.s^{-1}) and complexes 1a and 2b (>3.0 mm.s^{-1}), confirming their structural difference (porphyrinic vs pyridinic).

By either adsorption of an ORR species (here an *OH moiety) or a ligand (here SO_4) the oxidation state of iron increases from Fe^{II} to Fe^{III}. The computed ΔE_{QS} values in Table S6 indicate that there is a significant difference between the obtained ΔE_{QS} values for the five-fold coordinated FeN_4 catalysts (rows 1-3) in S= 5/2 (<0.9 mm.s^{-1}) with other spin states (1.0<ΔE_{QS}<2.7 mm.s^{-1}). The quadrupole splitting values in S=5/2 are in the range of the experimental values reported in previous investigations [32, 37, 68], assigning the spin state of Fe^{III} to all the five-fold coordinated FeN_4 catalysts and consequently the switching behavior of Fe atom in FeN_4 catalysts during the ORR process (see Figure 5).

Finally, we calculated ΔE_{QS} for complexes 1a, 2b, and 1c with six-fold coordination as a representative of other complexes with similar coordination. In these complexes, the iron atom binds with four N atoms, one *OH group, and a ligand group. The computed ΔE_{QS} for S=0 is in the range of 1.8 – 2.3 mm.s^{-1} and for S=1 it is in the range of 0.2 – 2.5 mm.s^{-1}(rows 4-8). Therefore, we conclude that S=0 is in closer agreement with the reported experimental data

confirming the switching behavior of the Fe oxidation state from Fe^{III} to Fe^{II} in the six-fold coordinated FeN_4 catalysts.
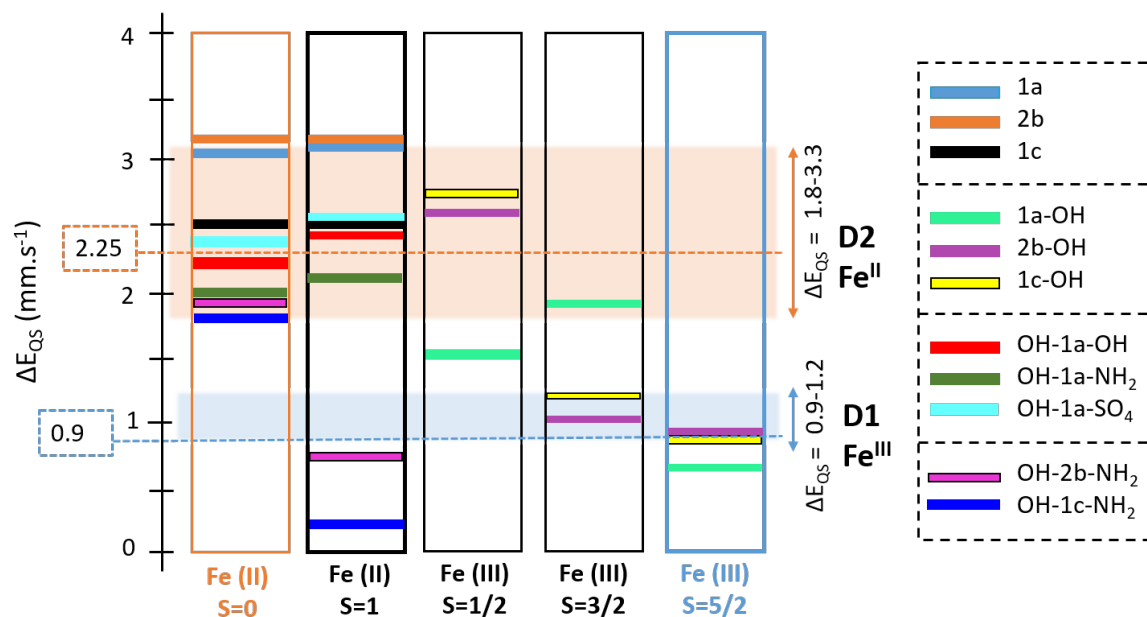

Figure 5. DFT calculated and measured ΔE_{QS} for FeN_4C_8, FeN_4C_{10}, and FeN_4C_{12} catalysts with four, five, and six-fold coordination. The blue and orange shaded areas represent the experimentally measured distribution of doublets D1 and D2, respectively. The dashed lines refer to the center of the fitted Gaussian distribution as reported in Ref [37].

According to Figure 5, the experimental doublet D1 can only be assigned to the five-fold coordinated FeN_4 structures. Among the studied catalysts, center of the D1 distribution corresponds best to the high-spin FeN_4C_{12} catalyst (S=5/2) with the mean ΔE_{QS} value of 0.9 mm.s^{-1}. It was reported that the doublet D2 (S2) is durable with no active site degradation after 50 h operation at 0.5 V [38]. We confirm this durability by assigning doublet D2 to pure FeN_4 catalysts before entering the ORR cycle and the six-fold coordinated structures. The oxidation number of iron in these configurations is Fe^{II}. The calculated ΔE_{QS} values for pure FeN_4 catalysts are all in the range of experimental values shown in the orange shaded region confirming that before starting the reduction reaction, the catalysts are ferrous rich. In the six-fold coordinated FeN_4 structures with S=0, all complexes are in the same range, although pyridinic complexes are the closest in value to the proposed range of 1.8-3.3 mm.s^{-1}. As

expected, complex 1a corresponds best to the mean ΔE_{QS} value of 2.2 mm.s^{-1}, confirming its high ORR activity.

Conclusions

The stability and durability of FeN$_4$ catalysts with different C-coordinations (FeN$_4$C$_8$, FeN$_4$C$_{10}$, and FeN$_4$C$_{12}$) were investigated ab initio using DFT-based modeling and Mössbauer characterization. Simulated Mössbauer spectra allowed us to identify FeN$_4$ pyridinic moieties (FeN$_4$C$_8$, FeN$_4$C$_{10}$) as well as the active porphyrinic FeN$_4$ sites (FeN$_4$C$_{12}$). Three major steps were analyzed carefully. (i) Before entering the ORR cycle the four-fold coordinated FeN$_4$ catalyst with extensive ferrous sites. (ii) The five-fold coordinated FeN$_4$ site with oxygenated intermediates adsorbed on the Fe atom, which forms during the reduction process. In this case, the ferrous ions directly or indirectly degrade into the ferric oxides leading to the demetallation of the catalyst; and (iii), ORR in the presence of the fifth ligand (NH_2^-, OH^-, and SO_4^{2-}), which changes the symmetry of the configuration and the iron-coordination to ferric by forming a six-fold coordinated FeN$_4$, and it is found to be surprisingly ORR active. The mechanism is that the fifth ligand pulls back the Fe atom into the basal plane upon adsorption of the ORR intermediates and prevents the elongation of the Fe-N bond and thus reduces the degradation of the catalyst. The pyridinic FeN$_4$C$_8$ catalyst is found to exhibit both durability and ORR activity in the presence of the fifth ligand. Our study provides a new pathway for the rational design of robust FeN$_4$ catalysts for electrocatalysis and energy-conversion applications.

Supporting Information.

(a) The proposed FeN$_2$C$_4^+$ as the high temperature catalytic site (Figure 1 of ref [12]). (b) Visualization of the reaction of porphyrin with the carbon support (Figure 9 of ref. [14]). (c) the proposed structure of the Fe-N$_{2+2}$/C (Figure 12 of ref. [18]). All figures have been reproduced with the permission of the American Chemical Society. Possible structure of most of the catalytic sites in Fe/N/C catalysts. Reprinted from ref. [22]. Copyright (2008), with permission from Elsevier. Comparison between the experimental K-edge XANES spectrum of Fe$_{0.5}$ (black dashed lines) with the theoretical spectrum calculated based on the depicted structures (solid red lines) for the proposed (a) FeN$_4$C$_{10}$, (b) FeN$_{2+2}$C$_{4+4}$, and (c) FeN$_4$C$_{12}$

moieties. Color code: gray, C; blue, N; orange, Fe. Copyright (2015), reproduced with permission from Nature. DFT calculations. Models for FeN4C catalysts. Free energy calculations. Mössbauer calculations. Origin of Quadrupole splitting. Calculated total density-of-state (DOS) for the complexes 1a, 1b, 1c, 2a and 2b. The most stable optimized configurations of ORR intermediate species adsorbed on complexes 2a and 1b. Color code: brown, C; blue, N; orange, Fe; white, H; and red, O. Binding energies of ORR species on complexes 1a, 1c, 2a, and 2b. Calculated total and partial densities of states for the adsorbed configurations of *OH on complexes 1a, 1b, 1c, 2a, 2b and 1a, 2b, 1c, respectively. Optimized adsorption configurations of NH_2^-, OH^-, and SO_4^{2-} on periodic FeN_4C_8, complex 2a. Color code: brown, C; blue, N; orange, Fe; white, H; red, O; and yellow, S. Calculated binding energies of ligands on complexes 1a, 2a, 2b, and 1c. The most stable optimized structures of ORR intermediate species adsorbed on complexes 1a, 2b, and 1c in the presence of the fifth ligand. Color code: brown, C; blue, N; orange, Fe; and white, H; red, O; yellow, S. Calculated adsorption energies of ORR intermediate species on complexes 1a, 2b, and 1c in the presence of the fifth ligand. Calculated free-energy evolution diagram for ORR on complexes 1a (a), 2b (b), and 1c (c) in the presence of NH_2^-, OH^-, and SO4^{2-} ligands at zero potential. Computed average Fe-N (d_{Fe-N}) and Fe-O (d_{Fe-O}) bond length of ORR intermediates on FeN_4C_x (x = 8, 10, and 12), the corresponding adsorption energy (E_{ads}), the ORR limiting potential (U_{lim}), along with the calculated overpotential (η). Bond lengths, energies, and potentials are in Å, eV, and V, respectively. Computed adsorption energies (E_{ads}) and changes in the Gibbs free energies (ΔG_{ads}) of ORR intermediates on FeN_4C_x (x = 8, 10, and 12). Computed adsorption energies (E_{ads}) of the ligands and ORR intermediate species on FeN_4 substrates. Magnetic moment (in units of Bohr magneton, **μ_B**) of the Fe atom in complexes 2a, 2b, and 1c before and after ORR with and without the fifth ligand. Values in parenthesis give the total magnetic moments. Quadrupole-splitting energy (ΔE_{QS}) in mm.s^{-1} for the catalysts containing ferrous moieties. Quadrupole-splitting energy (ΔE_{QS}) in mm.s^{-1} for the catalysts containing ferric moieties.

References

[1] F.T. Wagner, B. Lakshmanan, M.F. Mathias, Electrochemistry and the future of the automobile, J. Phys. Chem. Lett., 1 (2010) 2204-2219.

[2] Y. Wang, J. Li, Z. Wei, Transition-metal-oxide-based catalysts for the oxygen reduction reaction, J. Mater. Chem. A, 6 (2018) 8194-8209.

[3] L. Zhao, Y. Zhang, L.-B. Huang, X.-Z. Liu, Q.-H. Zhang, C. He, Z.-Y. Wu, L.-J. Zhang, J. Wu, W. Yang, Cascade anchoring strategy for general mass production of high-loading single-atomic metal-nitrogen catalysts, Nat. Commun., 10 (2019) 1-11.

[4] Y. Shao, J.P. Dodelet, G. Wu, P. Zelenay, PGM-Free Cathode Catalysts for PEM Fuel Cells: A Mini-Review on Stability Challenges, Adv. Mater., 31 (2019) e1807615.

[5] T. Okada, M. Yoshida, T. Hirose, K. Kasuga, T. Yu, M. Yuasa, I. Sekine, Oxygen reduction characteristics of graphite electrodes modified with cobalt di-quinolyldiamine derivatives, Electrochim. Acta, 45 (2000) 4419-4429.

[6] G.-Q. Sun, J.-T. Wang, S. Gupta, R. Savinell, Iron (III) tetramethoxyphenylporphyrin (FeTMPP-C1) as electrocatalyst for oxygen reduction in direct methanol fuel cells, J. Appl. Electrochem., 31 (2001) 1025-1031.

[7] O. Contamin, C. Debiemme-Chouvy, M. Savy, G. Scarbeck, O~ 2 electroreduction catalysis: effects of sulfur addition on some cobalt macrocycles, Journal of New Materials for Electrochemical Systems, 3 (2000) 67-74.

[8] M. Lefevre, J. Dodelet, P. Bertrand, O2 reduction in PEM fuel cells: activity and active site structural information for catalysts obtained by the pyrolysis at high temperature of Fe precursors, J. Phys. Chem. B., 104 (2000) 11238-11247.

[9] S. Kim, Applications of synchrotron radiation and optical spectroscopic techniques to the study of electrochemical interfaces, Case Western Reserve University, 1993.

[10] G. Wei, J. Wainright, R. Savinell, Catalytic activity for oxygen reduction reaction of catalysts consisting of carbon, nitrogen and cobalt, Journal of New Materials for Electrochemical Systems, 3 (2000) 121-130.

[11] G. Faubert, R. Côté, D. Guay, J. Dodelet, G. Denes, C. Poleunis, P. Bertrand, Activation and characterization of Fe-based catalysts for the reduction of oxygen in polymer electrolyte fuel cells, Electrochim. Acta, 43 (1998) 1969-1984.

[12] M. Lefèvre, J. Dodelet, P. Bertrand, Molecular oxygen reduction in PEM fuel cells: evidence for the simultaneous presence of two active sites in Fe-based catalysts, J. Phys. Chem. B., 106 (2002) 8705-8713.

[13] J.H. Zagal, F. Bedioui, J.-P. Dodelet, N4-macrocyclic metal complexes, Springer Science & Business Media2007.

[14] A. Bouwkamp-Wijnoltz, W. Visscher, J. Van Veen, E. Boellaard, A. Van der Kraan, S. Tang, On active-site heterogeneity in pyrolyzed carbon-supported iron porphyrin catalysts for the electrochemical reduction of oxygen: an in situ Mössbauer study, J. Phys. Chem. B., 106 (2002) 12993-13001.

[15] M. Bron, S. Fiechter, M. Hilgendorff, P. Bogdanoff, Catalysts for oxygen reduction from heat-treated carbon-supported iron phenantroline complexes, J. Appl. Electrochem., 32 (2002) 211-216.

[16] M. Bron, J. Radnik, M. Fieber-Erdmann, P. Bogdanoff, S. Fiechter, EXAFS, XPS and electrochemical studies on oxygen reduction catalysts obtained by heat treatment of iron phenanthroline complexes supported on high surface area carbon black, Journal of Electroanalytical Chemistry, 535 (2002) 113-119.

[17] M. Bron, S. Fiechter, P. Bogdanoff, H. Tributsch, Thermogravimetry/Mass Spectrometry Investigations on the Formation of Oxygen Reduction Catalysts for PEM Fuel Cells on the

Basis of Heat‑Treated Iron Phenanthroline Complexes, Fuel Cells, 2 (2002) 137-142.

[18] H. Schulenburg, S. Stankov, V. Schünemann, J. Radnik, I. Dorbandt, S. Fiechter, P. Bogdanoff, H. Tributsch, Catalysts for the oxygen reduction from heat-treated iron (III) tetramethoxyphenylporphyrin chloride: structure and stability of active sites, J. Phys. Chem. B., 107 (2003) 9034-9041.

[19] G. Zhutaeva, K. Radyushkina, M. Marinich, G. Bogatyreva, M. Tarasevich, Electrocatalysis of the oxygen reaction on electrodes prepared using disperse synthetic diamond promoted with cobalt porphyrin and its pyropolymer, Russian journal of electrochemistry, 37 (2001) 1059-1064.

[20] F. Jaouen, S. Marcotte, J.-P. Dodelet, G. Lindbergh, Oxygen reduction catalysts for polymer electrolyte fuel cells from the pyrolysis of iron acetate adsorbed on various carbon supports, J. Phys. Chem. B., 107 (2003) 1376-1386.

[21] D. Villers, X. Jacques-Bédard, J.-P. Dodelet, Fe-based catalysts for oxygen reduction in PEM fuel cells: pretreatment of the carbon support, J. Electrochem. Soc., 151 (2004) A1507.

[22] F. Charreteur, F. Jaouen, S. Ruggeri, J.-P. Dodelet, Fe/N/C non-precious catalysts for PEM fuel cells: Influence of the structural parameters of pristine commercial carbon blacks on their activity for oxygen reduction, Electrochim. Acta, 53 (2008) 2925-2938.

[23] M. Lefèvre, E. Proietti, F. Jaouen, J.-P. Dodelet, Iron-based catalysts with improved oxygen reduction activity in polymer electrolyte fuel cells, Science, 324 (2009) 71-74.

[24] A. Zitolo, V. Goellner, V. Armel, M.-T. Sougrati, T. Mineva, L. Stievano, E. Fonda, F. Jaouen, Identification of catalytic sites for oxygen reduction in iron-and nitrogen-doped graphene materials, Nat. Mater., 14 (2015) 937-942.

[25] G. Xiao, R. Lu, J. Liu, X. Liao, Z. Wang, Y. Zhao, Coordination environments tune the activity of oxygen catalysis on single atom catalysts: A computational study, Nano Res., (2021) 1-9.

[26] H. Jing, P. Zhu, X. Zheng, Z. Zhang, D. Wang, Y. Li, Theory-oriented screening and discovery of advanced energy transformation materials in electrocatalysis, Advanced Powder Materials, 1 (2022) 100013.

[27] A.B. Anderson, E.F. Holby, Pathways for O2 Electroreduction over Substitutional FeN4, HOFeN4, and OFeN4 in Graphene Bulk Sites: Critical Evaluation of Overpotential Predictions Using LGER and CHE Models, J. Phys. Chem. C., 123 (2019) 18398-18409.

[28] G. Zhu, F. Liu, Y. Wang, Z. Wei, W. Wang, Systematic exploration of N, C coordination effects on the ORR performance of Mn–N x doped graphene catalysts based on DFT calculations, Phys. Chem. Chem. Phys., 21 (2019) 12826-12836.

[29] Y. Han, Y. Wang, R. Xu, W. Chen, L. Zheng, A. Han, Y. Zhu, J. Zhang, H. Zhang, J. Luo, Electronic structure engineering to boost oxygen reduction activity by controlling the coordination of the central metal, Energy Environ. Sci., 11 (2018) 2348-2352.

[30] Q. Jia, N. Ramaswamy, H. Hafiz, U. Tylus, K. Strickland, G. Wu, B. Barbiellini, A. Bansil, E.F. Holby, P. Zelenay, Experimental observation of redox-induced Fe–N switching behavior as a determinant role for oxygen reduction activity, ACS Nano, 9 (2015) 12496-12505.

[31] C.J. Pollock, M.U. Delgado-Jaime, M. Atanasov, F. Neese, S. DeBeer, Kβ mainline X-ray emission spectroscopy as an experimental probe of metal–ligand covalency, Journal of the American Chemical Society, 136 (2014) 9453-9463.

[32] M.T. Sougrati, V. Goellner, A.K. Schuppert, L. Stievano, F. Jaouen, Probing active sites in iron-based catalysts for oxygen electro-reduction: A temperature-dependent 57Fe Mössbauer spectroscopy study, Catal. Today, 262 (2016) 110-120.

[33] U.I. Kramm, L. Ni, S. Wagner, 57Fe mössbauer spectroscopy characterization of electrocatalysts, Adv. Mater., 31 (2019) 1805623.

[34] V.A. Saveleva, K. Ebner, L. Ni, G. Smolentsev, D. Klose, A. Zitolo, E. Marelli, J. Li, M. Medarde, O.V. Safonova, Potential‑Induced Spin Changes in Fe/N/C Electrocatalysts

Assessed by In Situ X‑ray Emission Spectroscopy, Angew. Chemi., 133 (2021) 11813-11818.

[35] U.I. Kramm, J. Herranz, N. Larouche, T.M. Arruda, M. Lefevre, F. Jaouen, P. Bogdanoff, S. Fiechter, I. Abs-Wurmbach, S. Mukerjee, Structure of the catalytic sites in Fe/N/C-catalysts for O 2-reduction in PEM fuel cells, Phys. Chem. Chem. Phys., 14 (2012) 11673-11688.

[36] U.I. Kramm, M. Lefèvre, N. Larouche, D. Schmeisser, J.-P. Dodelet, Correlations between mass activity and physicochemical properties of Fe/N/C catalysts for the ORR in PEM fuel cell via 57Fe Mossbauer spectroscopy and other techniques, Journal of the American Chemical Society, 136 (2014) 978-985.

[37] T. Mineva, I. Matanovic, P. Atanassov, M.-T. Sougrati, L. Stievano, M. Clémancey, A. Kochem, J.-M. Latour, F. Jaouen, Understanding active sites in pyrolyzed Fe–N–C catalysts for fuel cell cathodes by bridging density functional theory calculations and 57Fe Mossbauer spectroscopy, ACS Catal., 9 (2019) 9359-9371.

[38] J. Li, M.T. Sougrati, A. Zitolo, J.M. Ablett, I.C. Oğuz, T. Mineva, I. Matanovic, P. Atanassov, Y. Huang, I. Zenyuk, Identification of durable and non-durable FeN x sites in Fe–N–C materials for proton exchange membrane fuel cells, Nature Catalysis, 4 (2021) 10-19.

[39] G. Kresse, J. Hafner, Ab initio molecular dynamics for liquid metals, Phys. Rev. B, 47 (1993) 558.

[40] J. Perdew, K. Burke, M. Ernzerhof, D. of physics and NOL 70118 J. quantum theory group tulane university, Phys. Rev. Lett, 77 (1996) 3865-3868.

[41] G. Kresse, J. Furthmüller, Efficiency of ab-initio total energy calculations for metals and semiconductors using a plane-wave basis set, Comput. Mater. Sci., 6 (1996) 15-50.

[42] P.E. Blöchl, Projector augmented-wave method, Phys. Rev. B, 50 (1994) 17953.

[43] J.P. Perdew, J.A. Chevary, S.H. Vosko, K.A. Jackson, M.R. Pederson, D.J. Singh, C. Fiolhais, Atoms, molecules, solids, and surfaces: Applications of the generalized gradient approximation for exchange and correlation, Phys. Rev. B, 46 (1992) 6671.

[44] S. Grimme, Semiempirical GGA‑type density functional constructed with a long‑range dispersion correction, J. Comput. Chem., 27 (2006) 1787-1799.

[45] S. Grimme, J. Antony, S. Ehrlich, H. Krieg, A consistent and accurate ab initio parametrization of density functional dispersion correction (DFT-D) for the 94 elements H-Pu, J. Chem. Phys., 132 (2010) 154104-19.

[46] W. Tang, E. Sanville, G. Henkelman, A grid-based Bader analysis algorithm without lattice bias, J. Phys. Condens. Matter, 21 (2009) 084204.

[47] C. Rovira, K. Kunc, J. Hutter, P. Ballone, M. Parrinello, Equilibrium geometries and electronic structure of iron− porphyrin complexes: A density functional study, J. Phys. Chem. A., 101 (1997) 8914-8925.

[48] E.F. Holby, P. Zelenay, Linking structure to function: The search for active sites in non-platinum group metal oxygen reduction reaction catalysts, Nano Energy, 29 (2016) 54-64.

[49] C.E. Szakacs, M. Lefèvre, U.I. Kramm, J.-P. Dodelet, F. Vidal, A density functional theory study of catalytic sites for oxygen reduction in Fe/N/C catalysts used in H 2/O 2 fuel cells, Phys. Chem. Chem. Phys., 16 (2014) 13654-13661.

[50] K. Liu, G. Wu, G. Wang, Role of Local Carbon Structure Surrounding FeN4 Sites in Boosting the Catalytic Activity for Oxygen Reduction, J. Phys. Chem. C., 121 (2017) 11319-11324.

[51] U. Tylus, Q. Jia, K. Strickland, N. Ramaswamy, A. Serov, P. Atanassov, S. Mukerjee, Elucidating oxygen reduction active sites in pyrolyzed metal–nitrogen coordinated non-precious-metal electrocatalyst systems, J. Phys. Chem. C., 118 (2014) 8999-9008.

[52] S. Kattel, G. Wang, A density functional theory study of oxygen reduction reaction on Me–N4 (Me = Fe, Co, or Ni) clusters between graphitic pores, J. Mater. Chem. A, 1 (2013).

[53] U.I. Kramm, J. Herranz, N. Larouche, T.M. Arruda, M. Lefevre, F. Jaouen, P. Bogdanoff, S. Fiechter, I. Abs-Wurmbach, S. Mukerjee, J.P. Dodelet, Structure of the catalytic sites in

Fe/N/C-catalysts for O2-reduction in PEM fuel cells, Phys. Chem. Chem. Phys., 14 (2012) 11673-11688.

[54] S. Kattel, P. Atanassov, B. Kiefer, A density functional theory study of oxygen reduction reaction on non-PGM Fe–N x–C electrocatalysts, Phys. Chem. Chem. Phys., 16 (2014) 13800-13806.

[55] W.D. Edwards, B. Weiner, M.C. Zerner, On the low-lying states and electronic spectroscopy of iron (II) porphine, Journal of the American Chemical Society, 108 (1986) 2196-2204.

[56] L. Jiao, J. Li, L.L. Richard, Q. Sun, T. Stracensky, E. Liu, M.T. Sougrati, Z. Zhao, F. Yang, S. Zhong, Chemical vapour deposition of Fe–N–C oxygen reduction catalysts with full utilization of dense Fe–N4 sites, Nat. Mater., 20 (2021) 1385-1391.

[57] K. Kumar, L. Dubau, M. Mermoux, J. Li, A. Zitolo, J. Nelayah, F. Jaouen, F. Maillard, On the influence of oxygen on the degradation of Fe‐N‐C catalysts, Angew. Chemi., 132 (2020) 3261-3269.

[58] T.A. Albright, J.K. Burdett, M.-H. Whangbo, Orbital interactions in chemistry, John Wiley & Sons2013.

[59] R. Cao, R. Thapa, H. Kim, X. Xu, M.G. Kim, Q. Li, N. Park, M. Liu, J. Cho, Promotion of oxygen reduction by a bio-inspired tethered iron phthalocyanine carbon nanotube-based catalyst, Nat. Commun., 4 (2013) 1-7.

[60] E.F. Holby, C.D. Taylor, Activity of N-coordinated multi-metal-atom active site structures for Pt-free oxygen reduction reaction catalysis: role of *OH ligands, Sci. Rep., 5 (2015) 9286.

[61] D. Jain, Q. Zhang, V. Gustin, J. Hightower, S. Gunduz, A.C. Co, J.T. Miller, A. Asthagiri, U.S. Ozkan, Experimental and DFT Investigation into Chloride Poisoning Effects on Nitrogen-Coordinated Iron–Carbon (FeNC) Catalysts for Oxygen Reduction Reaction, J. Phys. Chem. C., 124 (2020) 10324-10335.

[62] B. Ge, B. Chen, L. Li, A DFT study on the relationship between local microstructure and oxygen reduction reaction activity over Fe-N4 graphene, Materials Today Communications, 25 (2020) 101524.

[63] J. Niemantsverdriet, A. Van der Kraan, W. Van Dijk, H. Van der Baan, Behavior of metallic iron catalysts during Fischer-Tropsch synthesis studied with Mossbauer spectroscopy, X-ray diffraction, carbon content determination, and reaction kinetic measurements, J. Phys. Chem., 84 (2002) 3363-3370.

[64] J. Souza, Extraterrestrial and terrestrial outdoor applications of Mössbauer spectroscopy, Johannes Gutenberg-Universität Mainz, 2004.

[65] P. Blaha, Calculations of Mössbauer parameters in solids by DFT bandstructure calculations, Journal of Physics: Conference Series, IOP Publishing, 2010, pp. 012009.

[66] M. Che, J.C. Védrine, Characterization of solid materials and heterogeneous catalysts: from structure to surface reactivity, John Wiley & Sons2012.

[67] P. Champion, R. Chiang, E. Münck, P. Debrunner, L. Hager, Mössbauer investigations of high-spin ferrous heme proteins. II. Chloroperoxidase, horseradish peroxidase, and hemoglobin, Biochemistry, 14 (1975) 4159-4166.

[68] U.I. Kramm, I. Herrmann-Geppert, J. Behrends, K. Lips, S. Fiechter, P. Bogdanoff, On an easy way to prepare metal–nitrogen doped carbon with exclusive presence of MeN4-type sites active for the ORR, Journal of the American Chemical Society, 138 (2016) 635-640.

Identification of a robust and durable FeN_4C_x catalyst for ORR in PEM fuel cells and the role of the fifth ligand

Parisa Nematollahi,[*,1] Bernardo Barbiellini,[2,3] Arun Bansil,[3] Dirk Lamoen,[4] Jia Qingying,[5] Sanjeev Mukerjee,[5] and Erik C. Neyts[1]

[1] Research Group PLASMANT, NANO lab Center of Excellence, Department of Chemistry, University of Antwerp, Universiteitsplein 1, B-2610 Wilrijk-Antwerp, Belgium

[2] Department of Physics, School of Engineering Science, LUT University, FI-53851 Lappeenranta, Finland

[3] Department of Physics, Northeastern University, Boston, MA 02115, USA

[4] EMAT & NanoLab Center of Excellence, Department of Physics, University of Antwerp, B-2020 Wilrijk-Antwerpen, Belgium

[5] Department of Chemistry and Chemical Biology, Northeastern University, Boston, MA 02115, USA

* Corresponding author. **Phone:** (+32) 32652346. **E-mail**: parisa.nematollahi@uantwerpen.be
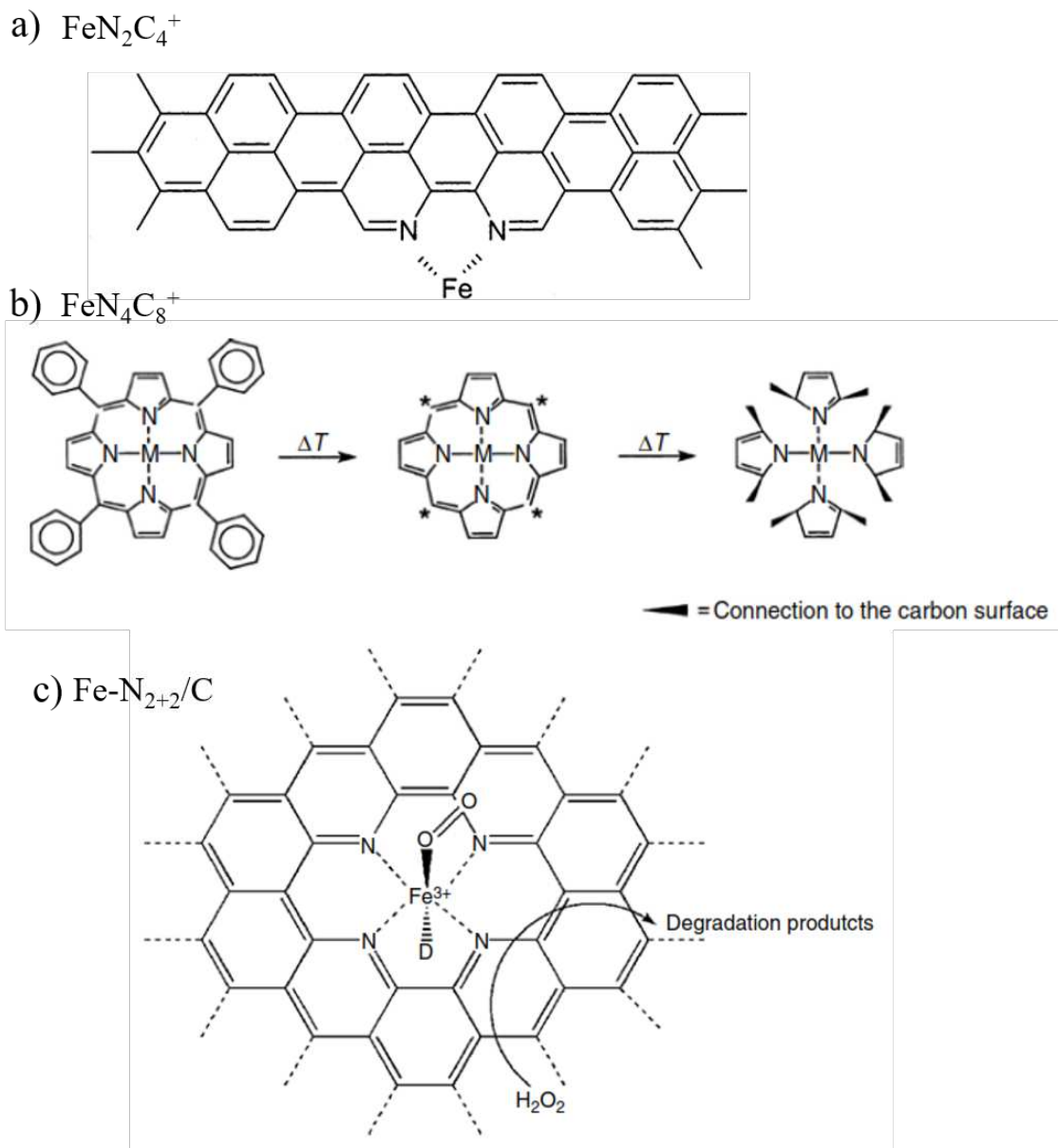
a) $FeN_2C_4^+$

b) $FeN_4C_8^+$

◀ = Connection to the carbon surface

c) $Fe-N_{2+2}/C$

Figure S1. (a)The proposed $FeN_2C_4^+$ as the high temperature catalytic site (Figure 1 of ref [1]). (b) Visualization of the reaction of porphyrin with the carbon support (Figure 9 of ref. [2]). (c) the proposed structure of the $Fe-N_{2+2}/C$ (Figure 12 of ref. [3]). All figures have been reproduced with the permission of the American Chemical Society.
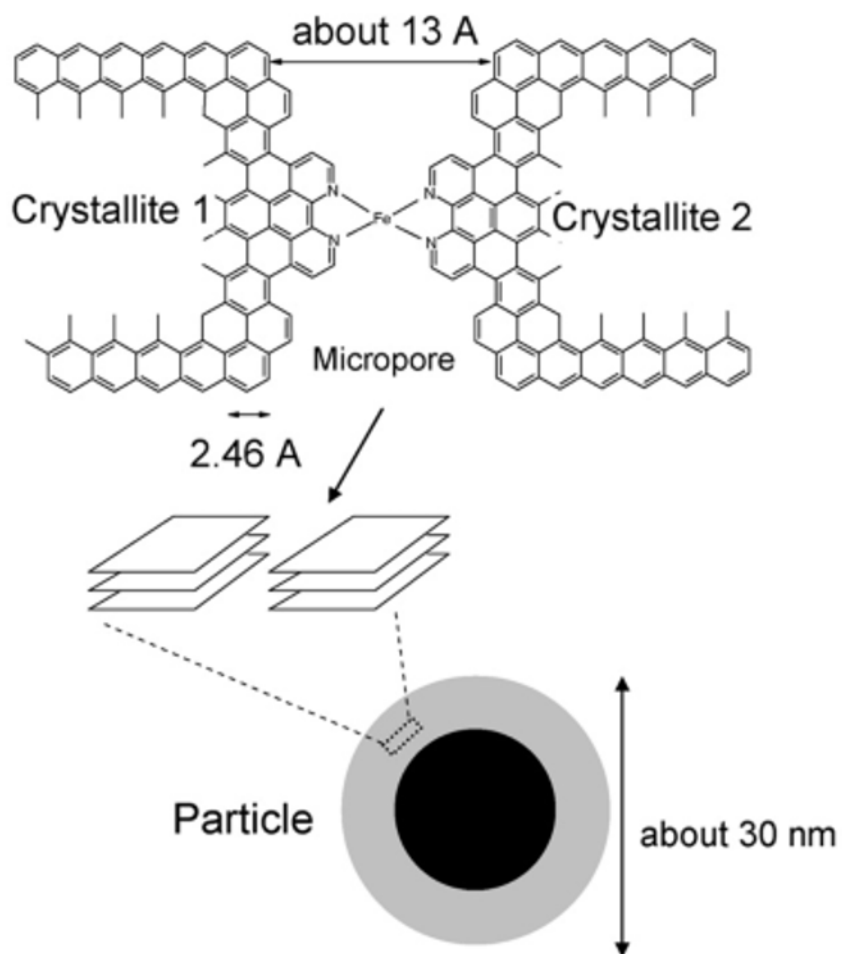
Figure S2. Possible structure of most of the catalytic sites in Fe/N/C catalysts. Reprinted from ref. [4]. Copyright (2008), with permission from Elsevier.
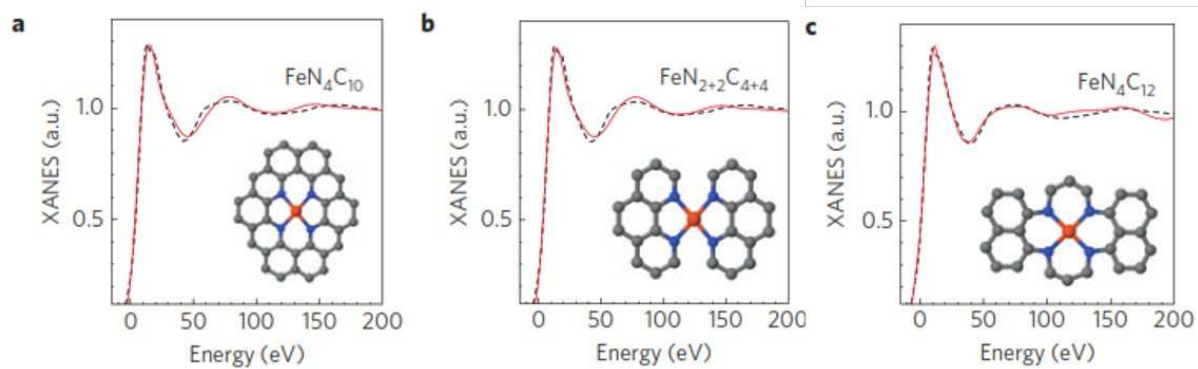
Figure S3. Comparison between the experimental K-edge XANES spectrum of $Fe_{0.5}$ (black dashed lines) with the theoretical spectrum calculated based on the depicted structures (solid red lines) for the proposed (a) FeN_4C_{10}, (b) $FeN_{2+2}C_{4+4}$, and (c) FeN_4C_{12} moieties. Color code: gray, C; blue, N; orange, Fe. Copyright (2015), reproduced with permission from Nature.

DFT calculations

The adsorption energy of adsorbates is obtained by using:

$$E_{ads} = E_{adsorbate@FeN4Cx} - (E_{adsorbate} + E_{FeN4Cx}) \tag{1}$$

where $E_{adsorbate@FeN4Cx}$, $E_{adsorbate}$, and E_{FeN4Cx} are the total energies of the FeN_4C_x surface with the adsorbed molecules, adsorbate, and the pure surface, respectively. An optimized O_2 molecule and the bulk Fe are used as a reference for evaluating the adsorption energy of atomic oxygen on the surface and Fe atom into the N_4 vacancies, respectively.

Models for FeN₄C catalysts

FeN₄C catalysts are well known as promising electrocatalysts for ORR. Recently, DFT calculations were used to examine various possible structures of the FeN_4 active site within the carbonic matrix [5-7]. However, there is no consensus on the local C structure surrounding the FeN_4 active site [8-11]. Five different FeN₄C models have been simulated with three different local C structures, i.e., cluster and periodic FeN_4C_8 (complexes 1a and 2a) and FeN_4C_{10} (complexes 1b and 2b), along with the FeN_4C_{12} cluster (complex 1c), representing the most common models found in the literature [12-16]. The atomistic configurations of complexes 2a and 2b are extended and shown in Figure S4. The porphyrin-like FeN₄ catalyst, complex 1c, was examined because of its stable structure and high performance in ORR [8, 17, 18]. All models are constructed by modifying a graphene layer with C−C bond length of 1.42 Å. For the FeN_4C_8 cluster (complex 1a), a planar 14.37 Å × 17.01 Å unit cell is used while for the FeN_4C_{10} and FeN_4C_{12} clusters, (complexes1b and 1c), a planar 24.55 Å ×34.03 Å unit cell is used. For the periodic FeN_4C_8 and FeN_4C_{10} (complexes 2a and 2b), a 4×2 and 4×4 unit cell is used with a periodic graphene slab of 9.82 Å × 17.01 Å and 9.82 Å × 8.50 Å, respectively. The models used vacuum-layer separations of 15 and 20 Å in complexes 1a, 2a, and 2b and 1b, 1c, respectively. The cluster sizes used in simulations are sufficiently large to avoid lateral interactions since the distances between the two hydrogen atoms in x − y directions are 8 Å ×

10.25 Å, 12.51 Å × 20.82 Å, and 13.28 Å × 20.70 Å for the clusters 1a, 1b, and 1c, respectively. The Brillouin zone integration was performed using a Γ-centered Monkhorst−Pack mesh [19] with 5×5×1 k-points for the periodic complexes 2a and 2b, while for the clusters 1a, 1b, and 1c only the Γ-point was used. The positions of all atoms are fully relaxed during the optimization process.
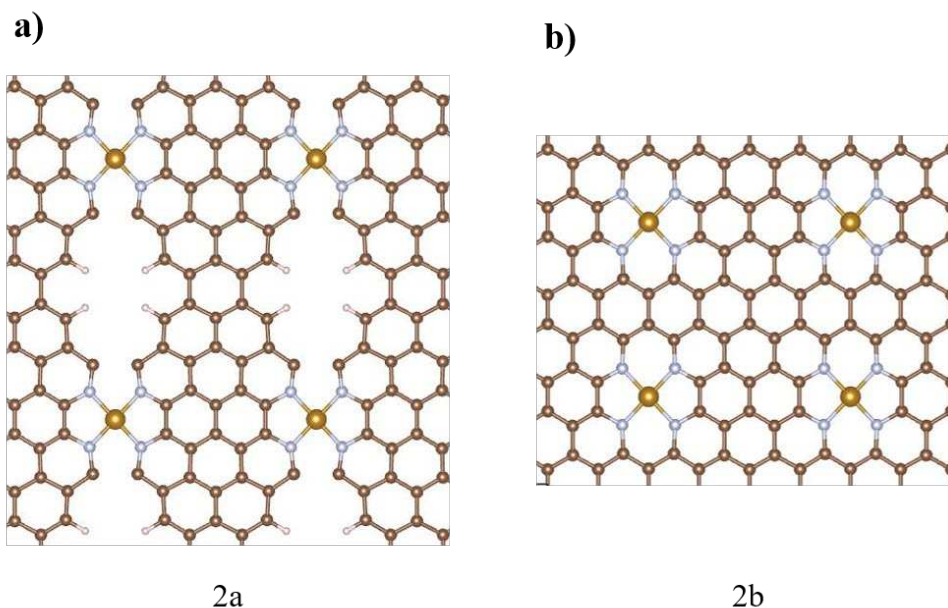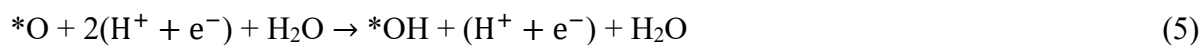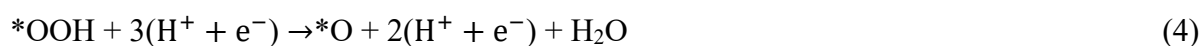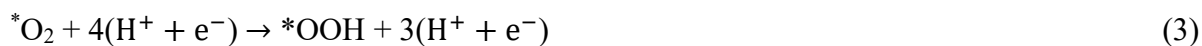
a)

b)

2a

2b

Figure S4. Atomistic configurations of FeN_4C_8 (a) and FeN_4C_{10} (b) active sites in extended simulation cells. Color code: brown, C; blue, N; orange, Fe; and white, H.

Free energy calculations

The method proposed by Nørskov et al. [20, 21] is used to calculate the free energy change of various elementary reactions occurring on the active site. The ORR reactions steps under acidic conditions are:

$$* + O_2\,(g) + 4(H^+ + e^-) \rightarrow O_2{}^* + 4(H^+ + e^-) \tag{2}$$

$$^*O_2 + 4(H^+ + e^-) \rightarrow {}^*OOH + 3(H^+ + e^-) \tag{3}$$

$$^*OOH + 3(H^+ + e^-) \rightarrow {}^*O + 2(H^+ + e^-) + H_2O \tag{4}$$

$$^*O + 2(H^+ + e^-) + H_2O \rightarrow {}^*OH + (H^+ + e^-) + H_2O \tag{5}$$

*OH + (H$^+$ + e$^-$) + H$_2$O → 2H$_2$O   (6)
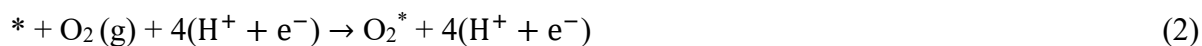
The free energy change for each reaction step can be expressed as:

ΔG = ΔE + ΔZPE – TΔS + ΔG$_{pH}$ + ΔG$_U$ (7)

where ΔE is the change in the total energy, ΔZPE is the change in the zero-point energy (ZPE), T is the temperature (298.15 K), and ΔS is the change in entropy. The ZPEs of the adsorbed ORR species were computed from DFT frequencies. For all adsorbed intermediates on FeN$_4$, only the vibrational entropy is taken into account because the translational and rotational degrees of freedom of the adsorbate effectively convert into vibrational modes (frustrated translations and rotations). Notably, for the gas phase molecules, the entropy term can be obtained by the sum of the translational, rotational, and vibrational contributions, whereas only the vibrational modes of the adsorbed species are computed explicitly, and the surface of the catalyst is fixed by assuming that the change in vibrations of the solid surface is negligible. ΔG$_{pH}$ refers to the correction of the H$^+$ free energy by the concentration: ΔG$_{pH}$ = 2.303 × k$_B$T × pH, where k$_B$ is the Boltzmann constant and the value of pH is set to be 0 in this work. ΔG$_U$ is the free energy contribution related to the applied electrode potential (U) versus the reversible hydrogen electrode (RHE), i.e., ΔG$_U$ = -neU, where n is the number of H$^+$/e$^-$ pairs transferred in NRR and e is the unit charge. The limiting potential (U$_{lim}$) is equal to $-$ΔG$_{min}$/e, where ΔG$_{min}$ is the step that releases the minimum energy among the four steps, i.e. the thermodynamic rate-determining step (RDS). Theoretical overpotential (η) is adopted as a measure of the whole ORR rate and determined as η = U$_{equ}$ – U$_{lim}$, where U$_{equ}$ is the equilibrium potential of ORR reaction, O$_2$(g) + 2H$^+$+2e^- → 2H$_2$O is 1.23 V vs. RHE, which is taken from the tabulated experimental standard reduction potentials [22, 23].

Mössbauer calculations

The electric field gradients (EFGs) at the positions of the Fe nuclei are calculated for all structures using VASP [24]. Cutoff energy of 400 eV and a Γ-point centered k-point mesh of

1×1×1 and 5×5×1 is chosen for cluster and periodic models, respectively. Convergence of the total energy was calculated using an energy cutoff in the range of 300-900 eV and the k-point sampling used meshes from 1×1×1 to 9×9×1 for periodic models. In all cases, the Fermi-Dirac smearing method with a sigma value of 0.03 eV was used [11].

Origin of Quadrupole splitting.

The quadrupole splitting energy can be obtained from the coupling between the nuclear quadrupole moment (Q) of the non-spherical nucleus and the principal components V_{ii} (I = x, y, z) of the EFG tensor at ^{57}Fe nucleus using:

$$\Delta E_{QS} = \frac{1}{2}eQV_{zz}\sqrt{1 + \frac{\eta^2}{3}} \tag{8}$$

Here e and Q are the elementary charge and nuclear quadrupole moment, respectively. The quadrupole moment of the excited ^{57}Fe nucleus is about 0.16 barn (1barn = 10^{-28} m^2) [25]. The EFG asymmetry parameter (η) is defined as $\eta = (V_{xx} - V_{yy})/V_{zz}$ where $|V_{zz}| \geq |V_{yy}| \geq V_{xx}$. In order to compare the computed ΔE_{QS} values with the corresponding experimental data, ΔE_{QS} is reported in units of mm/s. Calculation of ΔE_{QS} and η involves a computation of the EFG through the value of the EFG operator, $V_{ij} = \langle \Psi_0 | \frac{3ij - r^2}{r^5} | \Psi_0 \rangle$, for the electronic ground state Ψ_0 with i, j = x, y, z denoting components of the electron radius vector r.

The isomer shift (IS), δ, is related to the differences in electron density at the nucleus in the absorber (ρ_0^{sample}) and a reference ($\rho_0^{reference}$) compound (typically α-Fe) as [26]:

$$\delta = \alpha(\rho_0^{sample} - \rho_0^{reference})$$

where α is the so-called calibration constant ($\alpha = -0.1573\alpha_0^3 \, mm.\, s^{-1}$) which is determined from the experimental parameters of the ^{57}Fe nuclear transition [27] and ρ_0 is the nonrelativistic calculated total charge density at the iron nucleus.

Both QS and IS originate from the interaction between the charge densities of the iron nucleus and the surrounding electrons. The QS codes information about the electric field gradient (EFG). EFG is the degree of asymmetry within the electron density while IS gives the electron density at the iron nucleus also known as the contact density [28, 29]. However, although IS provides information about the iron oxidation and spin states, QS is not only sensitive to the

spin state but it can also help differentiate between various electronic states with the same multiplicity. Therefore, we only focused on QS for comparing our results with the experimental data.
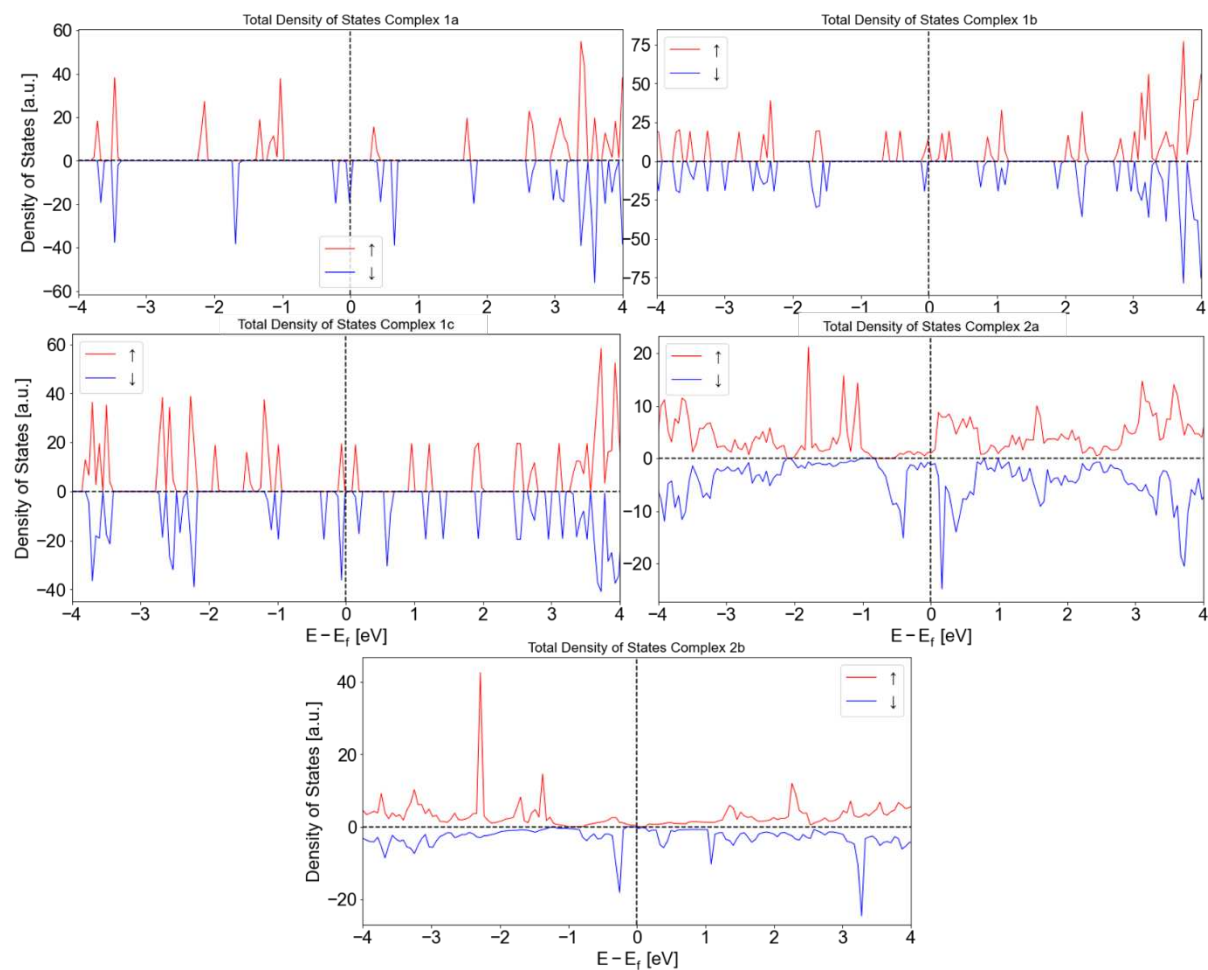

Figure S5. Calculated total density-of-state (DOS) for the complexes 1a, 1b, 1c, 2a and 2b.

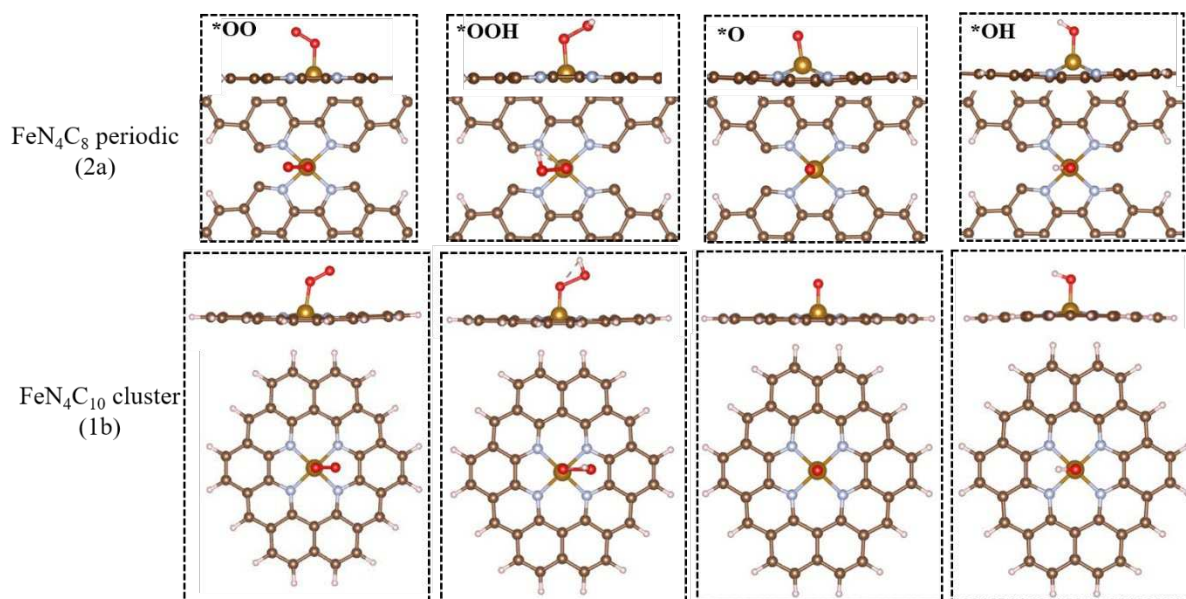**Figure S6.** The most stable optimized configurations of ORR intermediate species adsorbed on complexes 2a and 1b. Color code: brown, C; blue, N; orange, Fe; white, H; and red, O.
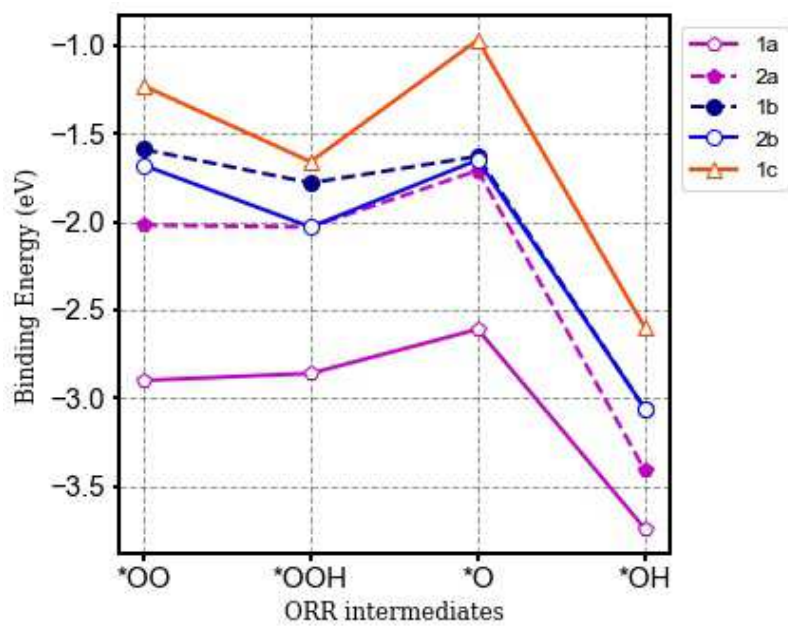
Figure S7. Binding energies of ORR species on complexes 1a, 1c, 2a, and 2b.
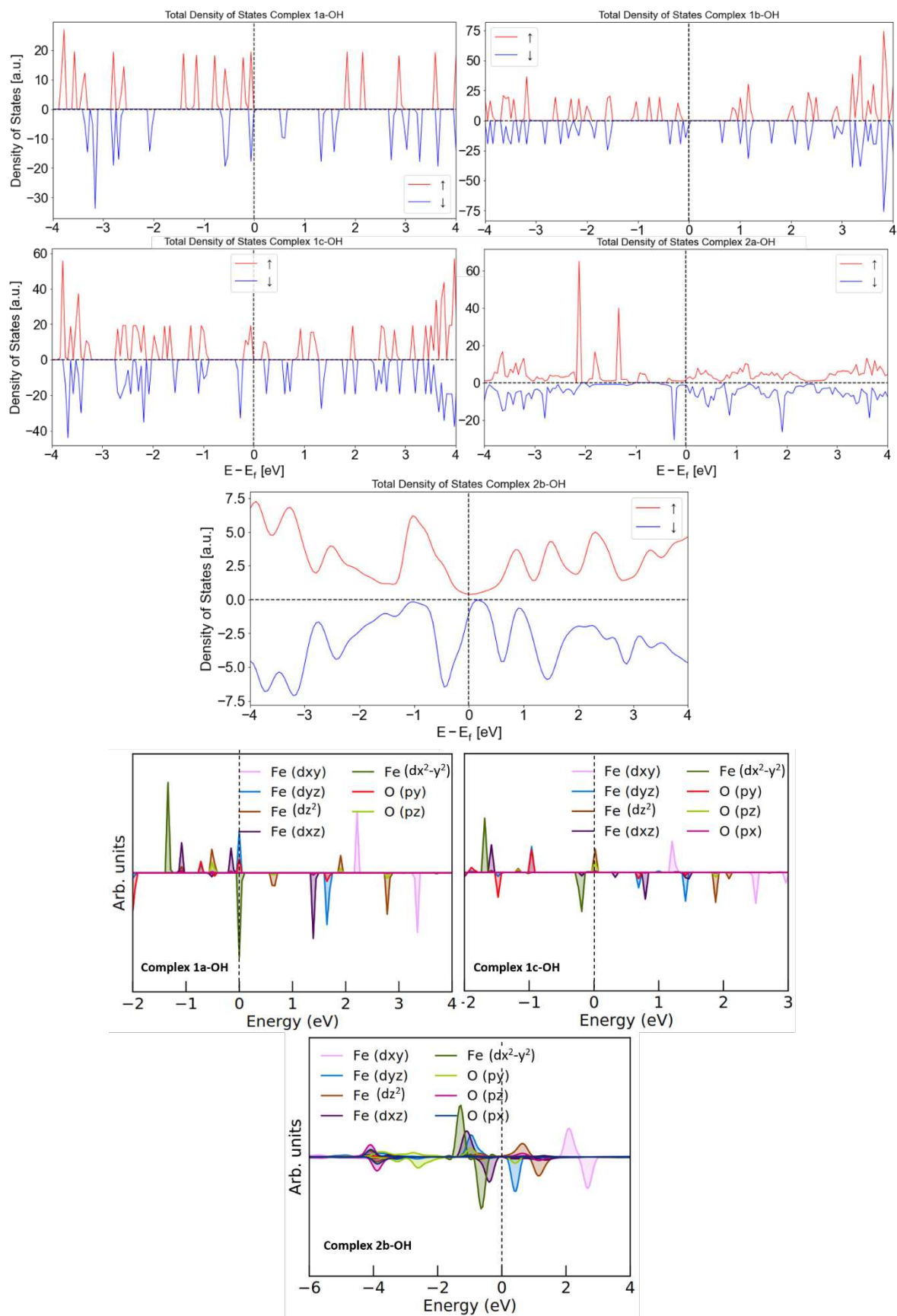
Figure S8. Calculated total and partial densities of states for the adsorbed configurations of *OH on complexes 1a, 1b, 1c, 2a, 2b and 1a, 2b, 1c, respectively.
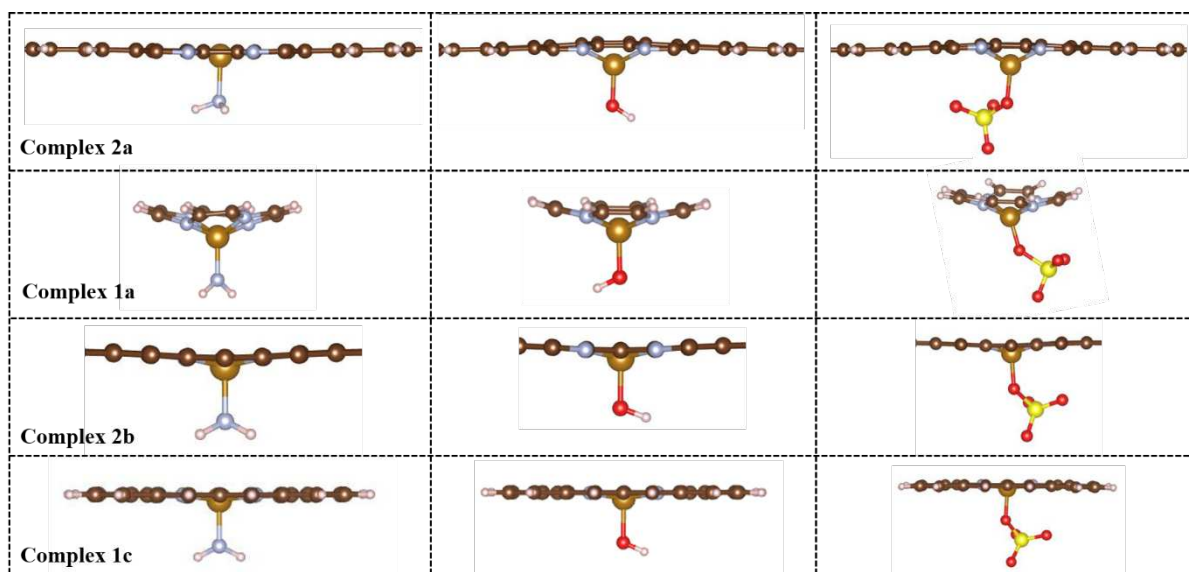
Figure S9. Optimized adsorption configurations of NH_2^-, OH^-, and SO_4^{2-} on periodic FeN$_4$C$_8$, complex 2a. Color code: brown, C; blue, N; orange, Fe; white, H; red, O; and yellow, S.
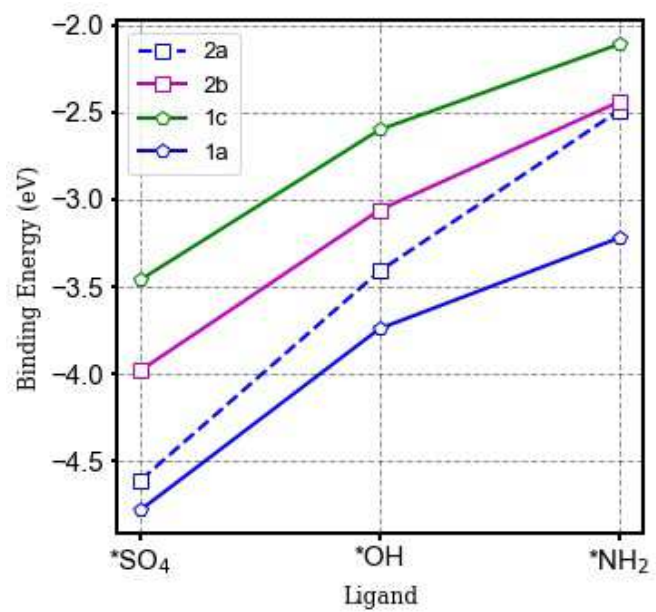
Figure S10. Calculated binding energies of ligands on complexes 1a, 2a, 2b, and 1c.
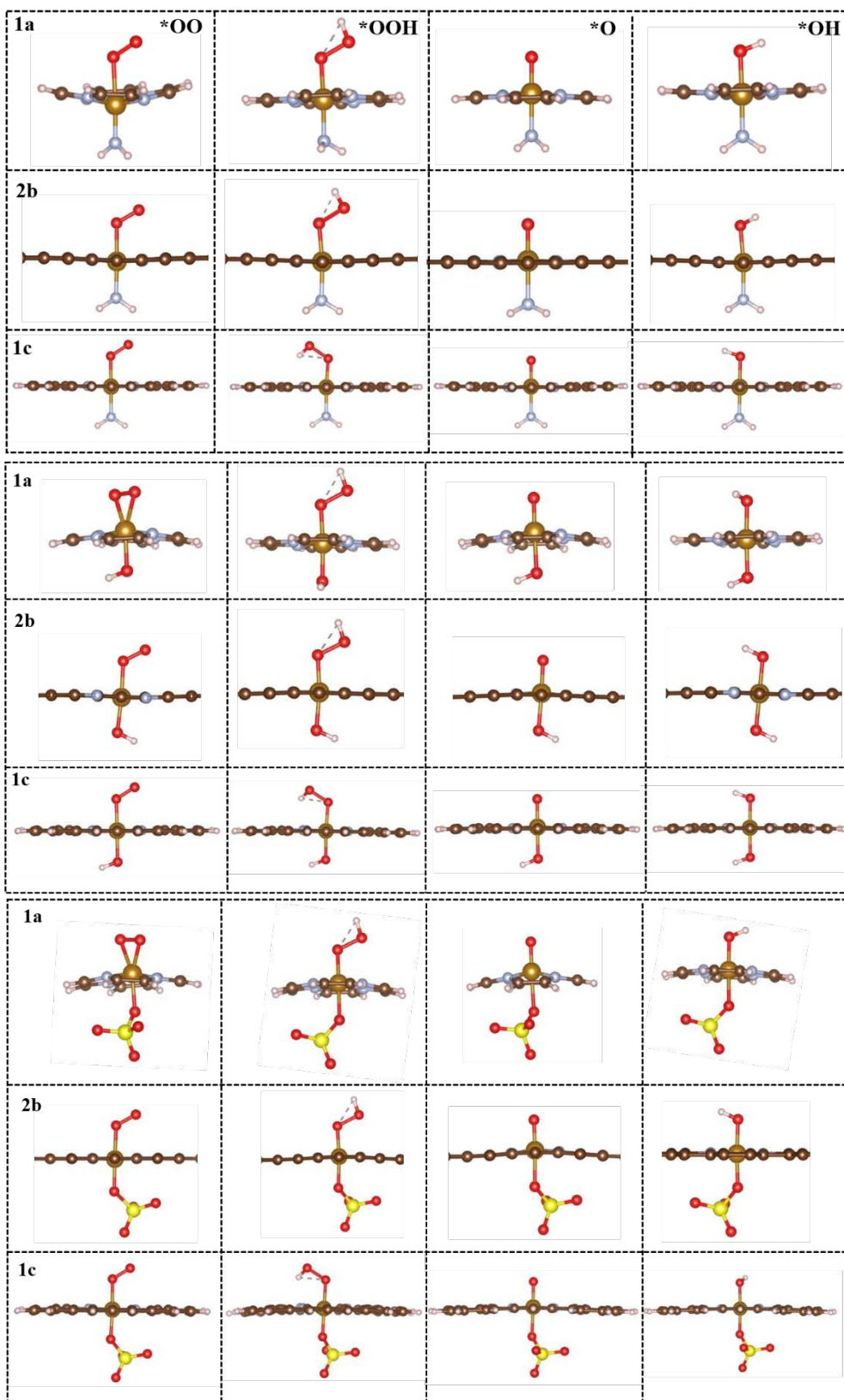
Figure S11. The most stable optimized structures of ORR intermediate species adsorbed on complexes 1a, 2b, and 1c in the presence of the fifth ligand. Color code: brown, C; blue, N; orange, Fe; and white, H; red, O; yellow, S.
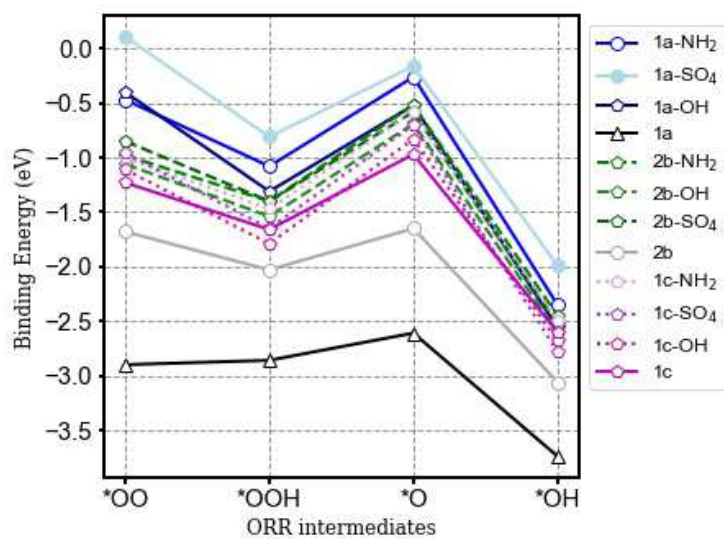
Figure S12. Calculated adsorption energies of ORR intermediate species on complexes 1a, 2b, and 1c in the presence of the fifth ligand
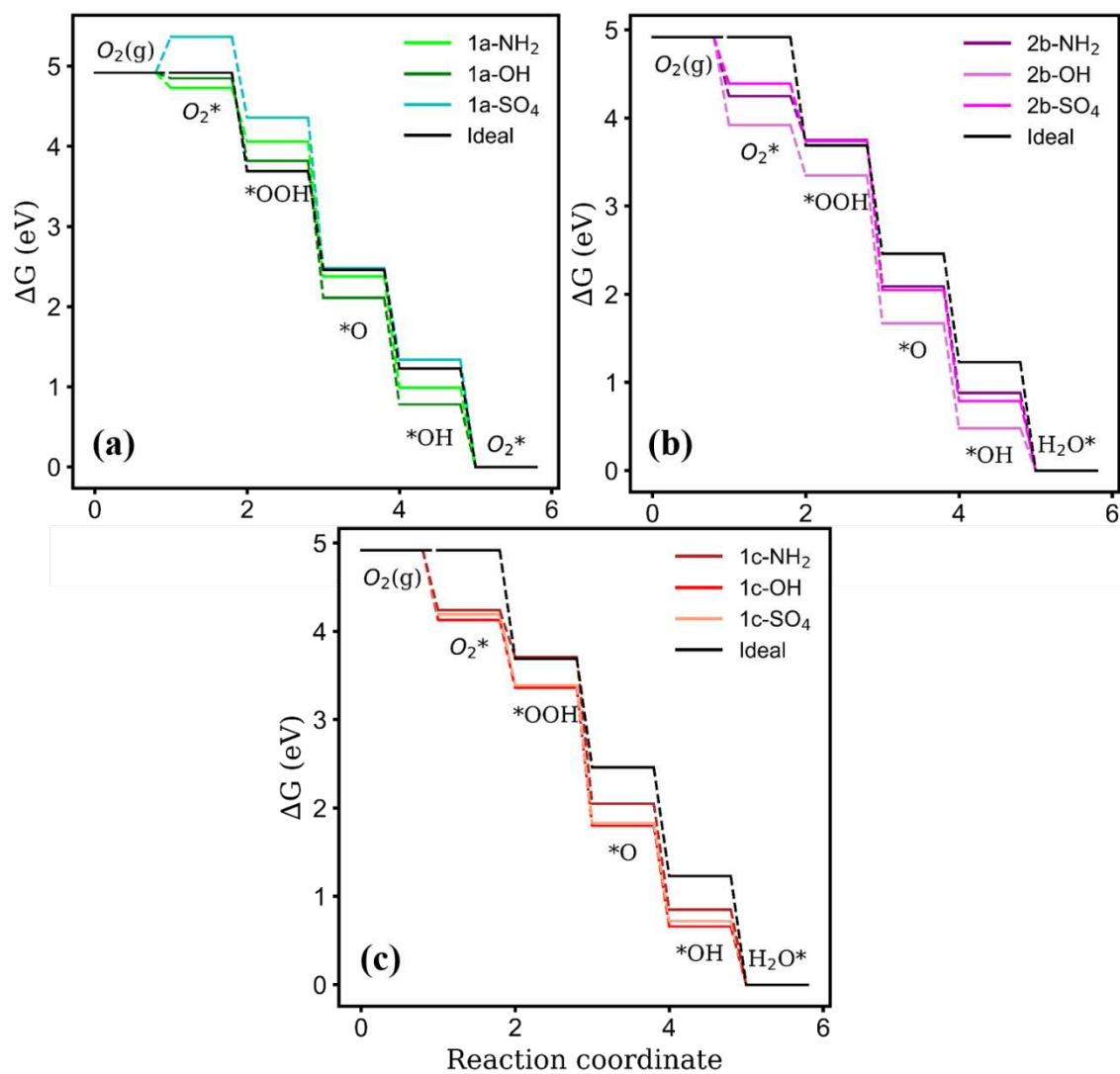
Figure S13. Calculated free-energy evolution diagram for ORR on complexes 1a (a), 2b (b), and 1c (c) in the presence of NH_2^-, OH^-, and SO_4^{2-} ligands at zero potential.

Table S1. Computed average Fe-N (d_{Fe-N}) and Fe-O (d_{Fe-O}) bond length of ORR intermediates on FeN$_4$C$_x$ (x = 8, 10, and 12), the corresponding adsorption energy (E_{ads}), the ORR limiting potential (U_{lim}), along with the calculated overpotential (η). Bond lengths, energies, and potentials are in Å, eV, and V, respectively.

| Complex		d_{Fe-N} (Å)					E_{ads}(eV)	U_{lim} (V)	η (V)
		Pure catalyst	O$_2$*	OOH*	O*	OH*			
FeN$_4$C$_8$	1a	1.85	1.88	1.87	1.85	1.89	-7.24	-0.42	1.65
	2a	1.84	1.85	1.87	1.97	1.97	-3.59	-0.11	1.12
1a	NH$_2$	1.83	1.84	1.86	1.87	1.86	-3.22	0.19	1.04
	OH	1.89	1.88	1.86	1.86	1.87	-3.74	0.07	1.16
	SO$_4$	1.85	1.83	1.84	1.87	1.84	-4.78	-0.45	1.68
FeN$_4$C$_{10}$	1b	1.89	1.91	1.91	1.92	1.90	-6.19	-	-
	2b	1.89	1.91	1.91	1.93	1.90	-6.49	0.25	0.98
2b	NH$_2$	1.91	1.91	1.90	1.92	1.91	-2.44	0.51	0.72
	OH	1.90	1.93	1.92	1.93	1.91	-3.06	0.48	0.75
	SO$_4$	1.93	1.91	1.92	1.94	1.93	-3.98	0.53	0.70
FeN$_4$C$_{12}$	1c	1.97	1.99	1.98	2.00	2.01	-10.32	0.55	0.68
1c	NH$_2$	1.99	1.99	2.00	2.00	2.00	-2.11	0.53	0.70
	OH	2.00	1.99	2.00	2.00	1.99	-2.60	0.66	0.57
	SO$_4$	1.98	2.00	2.01	2.02	2.02	-3.46	0.72	0.51

Complex		d_{Fe-O} (Å)			
		O$_2$*	OOH*	O*	OH*
FeN$_4$C$_8$	1a	1.85	2.83	1.61	1.82
	2a	1.82	1.84	1.63	1.82
1a	NH$_2$	2.19	1.88	1.64	1.86
	OH	1.89	1.87	1.63	1.85
	SO$_4$	1.89	1.81	1.62	1.82
FeN$_4$C$_{10}$	2b	1.74	1.75	1.64	1.80
2b	NH$_2$	1.97	1.87	1.68	1.89
	OH	1.92	1.84	1.68	1.87
	SO$_4$	1.92	1.83	1.66	1.85
FeN$_4$C$_{12}$	1c	1.83	1.74	1.63	1.88
1c	NH$_2$	1.89	1.81	1.64	1.83
	OH	1.82	1.86	1.66	1.86
	SO$_4$	1.79	1.86	1.64	1.83

Table S2. Computed adsorption energies (E_{ads}) and changes in the Gibbs free energies (ΔG_{ads}) of ORR intermediates on FeN$_4$C$_x$ (x = 8, 10, and 12)

Complex		E_{ads} and ΔG_{ads}	Adsorbed intermediate species			
			O_2*	OOH*	O*	OH*
FeN$_4$C$_8$	1a	E_{ads}	-2.90	-2.86	-2.61	-3.74
		ΔG_{ads}	-2.34	-2.22	-2.36	-3.15
	2a	E_{ads}	-2.02	-2.03	-1.71	-3.41
		ΔG_{ads}	-1.50	-1.48	-1.47	-2.85
FeN$_4$C$_{10}$	1b	E_{ads}	-1.59	-1.98	-1.63	-3.06
		ΔG_{ads}	-1.00	-1.20	-1.32	-2.61
	2b	E_{ads}	-1.68	-2.03	-1.65	-3.06
		ΔG_{ads}	-1.13	-1.44	-1.37	-2.48
FeN$_4$C$_{12}$	1c	E_{ads}	-1.23	-1.66	-0.97	-2.60
		ΔG_{ads}	-0.68	-1.08	-0.68	-2.02

Table S3. Computed adsorption energies (E_{ads}) of the ligands and ORR intermediate species on FeN_4 substrates.

Complex		E_{ads} (eV)				
		Pure catalyst	O_2*	OOH*	O*	OH*
1a (FeN_4C_8)	NH_2	-3.22	-0.47	-1.08	-0.26	-2.35
	OH	-3.74	-0.40	-1.31	-0.52	-2.56
	SO_4	-4.78	0.11	-0.81	-0.16	-1.99
2b (FeN_4C_{10})	NH_2	-2.44	-0.98	-1.40	-0.52	-2.45
	OH	-3.06	-1.06	-1.54	-0.69	-2.60
	SO_4	-3.98	-0.85	-1.40	-0.58	-2.53
1c (FeN_4C_{12})	NH_2	-2.11	-1.00	-1.47	-0.58	-2.50
	OH	-2.60	-1.11	-1.79	-0.83	-2.68
	SO_4	-3.46	-0.96	-1.65	-0.70	-2.78

Table S4. Magnetic moment (in units of Bohr magneton, μ_B) of the Fe atom in complexes 2a, 2b, and 1c before and after ORR with and without the fifth ligand. Values in parenthesis give the total magnetic moments.

Complex	Substrate	*OO	*OOH	*O	*OH
2a (FeN_4C_8)	1.16 (1)	2.03 (2.4)	2.67 (3.9)	1.76 (3.6)	2.76 (3.9)
2a-OH	2.77 (3.9)	0.71 (0.5)	0.79 (1.5)	1.25 (2.6)	0.95 (1.6)
2a-SO₄	3.10 (4.4)	2.07 (0.5)	1.63 (2.9)	1.13 (2)	1.78 (3)
2b (FeN_4C_{10})	1.74 (2)	0.33 (0)	1.00 (1)	2.00 (2)	1.00 (1)
2b-NH₂	0.90 (1.0)	0.65 (0.1)	0.64 (0.9)	1.03 (1.8)	0.80 (1)
2b-OH	1.00 (1)	0.74 (0.1)	0.74 (0.9)	1.07 (1.8)	0.97 (1.2)
2b-SO₄	2 (2)	0.95 (0.2)	0.95 (1.2)	1.06 (1.8)	1.31 (1.9)
1c (FeN_4C_{12})	1.78 (2)	1.04 (2)	0.94 (3)	0.00 (0)	2.25 (3)
1c-NH₂	0.98 (3)	1.05 (1)	0.11 (0)	0.79 (1.0)	0.13 (0)
1c-SO₄	0.34 (0)	0.00 (0)	1.18 (0)	0.94 (1)	1.37 (1)

Table S5. Quadrupole-splitting energy (ΔE_{QS}) in mm.s^{-1} for the catalysts containing ferrous moieties

Row	Complex	ΔE_{QS} (S=0)	ΔE_{QS} (S=1)
1	1a	3.1	3.2
2	2b	3.3	3.2
3	1c	2.5	2.5
4	OH-1a-NH$_2$	2.0	2.1
5	OH-1a-OH	2.2	2.4
6	OH-1a-SO$_4$	2.3	2.5
7	OH-2b-NH$_2$	2.0	0.8
8	OH-1c-NH$_2$	1.8	0.2

Table S6. Quadrupole-splitting energy (ΔE_{QS}) in mm.s^{-1} for the catalysts containing ferric moieties

Row	Complex	ΔE_{QS} (S=1/2)	ΔE_{QS} (S=3/2)	ΔE_{QS} (S=5/2)
1	1a-OH	1.5	1.9	0.7
2	2b-OH	2.6	1.0	0.9
3	1c-OH	2.7	1.2	0.9
4	1a-SO$_4$	1.4	1.9	0.5
5	2b-SO$_4$	2.3	1.4	0.7
6	1c-SO$_4$	2.4	2.3	1.2

References

[1] M. Lefèvre, J. Dodelet, P. Bertrand, Molecular oxygen reduction in PEM fuel cells: evidence for the simultaneous presence of two active sites in Fe-based catalysts, J. Phys. Chem. B., 106 (2002) 8705-8713.

[2] A. Bouwkamp-Wijnoltz, W. Visscher, J. Van Veen, E. Boellaard, A. Van der Kraan, S. Tang, On active-site heterogeneity in pyrolyzed carbon-supported iron porphyrin catalysts for the electrochemical reduction of oxygen: an in situ Mössbauer study, J. Phys. Chem. B., 106 (2002) 12993-13001.

[3] H. Schulenburg, S. Stankov, V. Schünemann, J. Radnik, I. Dorbandt, S. Fiechter, P. Bogdanoff, H. Tributsch, Catalysts for the oxygen reduction from heat-treated iron (III) tetramethoxyphenylporphyrin chloride: structure and stability of active sites, J. Phys. Chem. B., 107 (2003) 9034-9041.

[4] F. Charreteur, F. Jaouen, S. Ruggeri, J.-P. Dodelet, Fe/N/C non-precious catalysts for PEM fuel cells: Influence of the structural parameters of pristine commercial carbon blacks on their activity for oxygen reduction, Electrochim. Acta, 53 (2008) 2925-2938.

[5] S. Kattel, P. Atanassov, B. Kiefer, A density functional theory study of oxygen reduction reaction on non-PGM Fe–N x–C electrocatalysts, Phys. Chem. Chem. Phys., 16 (2014) 13800-13806.

[6] J. Zhang, Z. Wang, Z. Zhu, Q. Wang, A density functional theory study on mechanism of electrochemical oxygen reduction on FeN4-graphene, J. Electrochem. Soc., 162 (2015) F796.

[7] A. G. Saputro, H. Kasai, K. Asazawa, H. Kishi, H. Tanaka, Comparative study on the catalytic activity of the TM–N2 active sites (TM= Mn, Fe, Co, Ni) in the oxygen reduction reaction: density functional theory study, Journal of the Physical Society of Japan, 82 (2013) 114704.

[8] A. Zitolo, V. Goellner, V. Armel, M.-T. Sougrati, T. Mineva, L. Stievano, E. Fonda, F. Jaouen, Identification of catalytic sites for oxygen reduction in iron-and nitrogen-doped graphene materials, Nat. Mater., 14 (2015) 937-942.

[9] X. Wan, X. Liu, Y. Li, R. Yu, L. Zheng, W. Yan, H. Wang, M. Xu, J. Shui, Fe–N–C electrocatalyst with dense active sites and efficient mass transport for high-performance proton exchange membrane fuel cells, Nature Catalysis, 2 (2019) 259-268.

[10] L. Ni, C. Gallenkamp, S. Paul, M. Kübler, P. Theis, S. Chabbra, K. Hofmann, E. Bill, A. Schnegg, B. Albert, Active Site Identification in FeNC Catalysts and Their Assignment to the Oxygen Reduction Reaction Pathway by In Situ 57Fe Mössbauer Spectroscopy, Advanced Energy and Sustainability Research, 2 (2021) 2000064.

[11] T. Mineva, I. Matanovic, P. Atanassov, M.-T. Sougrati, L. Stievano, M. Clémancey, A. Kochem, J.-M. Latour, F. Jaouen, Understanding active sites in pyrolyzed Fe–N–C catalysts for fuel cell cathodes by bridging density functional theory calculations and 57Fe Mossbauer spectroscopy, ACS Catal., 9 (2019) 9359-9371.

[12] M. Wang, Z. Wang, Single Ni atom incorporated with pyridinic nitrogen graphene as an efficient catalyst for CO oxidation: first-principles investigation, RSC Adv., 7 (2017) 48819-48824.

[13] Y.-C. Lin, P.-Y. Teng, C.-H. Yeh, M. Koshino, P.-W. Chiu, K. Suenaga, Structural and chemical dynamics of pyridinic-nitrogen defects in graphene, Nano Lett., 15 (2015) 7408-7413.

[14] Z. Luo, S. Lim, Z. Tian, J. Shang, L. Lai, B. MacDonald, C. Fu, Z. Shen, T. Yu, J. Lin, Pyridinic N doped graphene: synthesis, electronic structure, and electrocatalytic property, J. Mater. Chem., 21 (2011) 8038-8044.

[15] C. Rovira, K. Kunc, J. Hutter, P. Ballone, M. Parrinello, Equilibrium geometries and electronic structure of iron− porphyrin complexes: A density functional study, J. Phys. Chem. A., 101 (1997) 8914-8925.

[16] Q. Jia, N. Ramaswamy, H. Hafiz, U. Tylus, K. Strickland, G. Wu, B. Barbiellini, A. Bansil, E.F. Holby, P. Zelenay, Experimental observation of redox-induced Fe–N switching behavior as a determinant role for oxygen reduction activity, ACS Nano, 9 (2015) 12496-12505.

[17] Z.S. Wu, L. Chen, J. Liu, K. Parvez, H. Liang, J. Shu, H. Sachdev, R. Graf, X. Feng, K. Müllen, High-performance electrocatalysts for oxygen reduction derived from cobalt porphyrin-based conjugated mesoporous polymers, Adv. Mater., 26 (2014) 1450-1455.

[18] H. Yang, R. Shi, L. Shang, T. Zhang, Recent Advancements of Porphyrin-Like Single-Atom Catalysts: Synthesis and Applications, Small Structures, 2 (2021) 2100007.

[19] H.J. Monkhorst, J.D. Pack, Special points for Brillouin-zone integrations, Phys. Rev. B, 13 (1976) 5188.

[20] J.K. Nørskov, J. Rossmeisl, A. Logadottir, L. Lindqvist, J.R. Kitchin, T. Bligaard, H. Jonsson, Origin of the overpotential for oxygen reduction at a fuel-cell cathode, J. Phys. Chem. B., 108 (2004) 17886-17892.

[21] A.A. Peterson, F. Abild-Pedersen, F. Studt, J. Rossmeisl, J.K. Nørskov, How copper catalyzes the electroreduction of carbon dioxide into hydrocarbon fuels, Energy Environ. Sci., 3 (2010) 1311-1315.

[22] G. Qing, R. Ghazfar, S.T. Jackowski, F. Habibzadeh, M.M. Ashtiani, C.-P. Chen, M.R. Smith III, T.W. Hamann, Recent advances and challenges of electrocatalytic N2 reduction to ammonia, Chem. Rev., 120 (2020) 5437-5516.

[23] J. Deng, J.A. Iñiguez, C. Liu, Electrocatalytic nitrogen reduction at low temperature, Joule, 2 (2018) 846-856.

[24] H.M. Petrilli, P.E. Blöchl, P. Blaha, K. Schwarz, Electric-field-gradient calculations using the projector augmented wave method, Phys. Rev. B, 57 (1998) 14690.

[25] P. Dufek, P. Blaha, K. Schwarz, Determination of the nuclear quadrupole moment of 57 Fe, Phys. Rev. Lett., 75 (1995) 3545.

[26] V.N. Nemykin, R.G. Hadt, Influence of Hartree− Fock Exchange on the Calculated Mössbauer Isomer Shifts and Quadrupole Splittings in Ferrocene Derivatives Using Density Functional Theory, Inorganic chemistry, 45 (2006) 8297-8307.

[27] G.K. Shenoy, F. Wagner, Mössbauer isomer shifts, (1978).

[28] P. Blaha, Calculations of Mössbauer parameters in solids by DFT bandstructure calculations, Journal of Physics: Conference Series, IOP Publishing, 2010, pp. 012009.

[29] C. Gallenkamp, U.I. Kramm, J. Proppe, V. Krewald, Calibration of computational Mössbauer spectroscopy to unravel active sites in FeNC catalysts for the oxygen reduction reaction, International Journal of Quantum Chemistry, 121 (2021) e26394.